Asymmetric Hill Equations Arising from Bilinear Oscillators with State-Dependent Parametric Excitation

Anish Kumar*

Department of Aerospace Engineering

Indian Institute of Space Science and Technology

Thiruvananthapuram, 695547, Kerala, India

July 13, 2026

Abstract

This study presents an analytical and numerical investigation of bilinear oscillators subjected to piecewise parametric excitation, where both the excitation amplitude and damping are state-dependent. The governing equations are formulated as asymmetric Hill's equations with asymmetric parametric excitation. The method of averaging is employed to derive the corresponding slow-flow equations, whose stability is analyzed and validated against direct numerical simulations. Closed-form expressions for the transition curves are developed, providing insight into instability boundaries for primary and subharmonic resonance conditions (1 : 1, 2 : 1, 3 : 1 and 4 : 1). The analysis is further extended to a physically relevant system—a cantilever beam with a breathing crack—demonstrating the equivalence between the asymmetric Hill model and structures with state-dependent stiffness and excitation. The proposed framework establishes an efficient approach for predicting dynamic instability in engineering systems exhibiting piecewise or state-dependent nonlinearities, such as beams and rotors with breathing cracks.

Keywords. Hill Equation, Bilinear Oscillator, Parametric Excitation, Piecewise Linear System, Breathing Vibrations.

*Corresponding Author: anishkumar@iist.ac.in (A. Kumar)

1 Introduction

The response of bilinear oscillatory systems subjected to various types of forcing has become a subject of immense theoretical and experimental research. These systems are commonly used to model the complex nonlinear responses of real engineering systems with intermittent contacts. For instance, the dynamics of articulated mooring towers [1], response of interlocking structures [2, 3], dynamics of suspension bridges [4–6], dynamics of mechanical structures with breathing cracks [7–9] can be effectively described by bilinear oscillatory models. A considerable amount of previous theoretical work has focused on both computational and analytical studies of resonant response of externally forced, single bilinear oscillator. Initial theoretical studies of the forced response of bilinear oscillators, have mainly focused on the construction of periodic solutions (see e.g., [10, 11]). Stability analysis and bifurcation analysis of steady state solutions of resonantly forced bilinear oscillator (PWLO) have been pursued in later computational and analytical studies by Thompson, Shaw and Holmes [12–14]. The first extensive computational and analytical studies of sub-harmonic resonances, bifurcations of periodic orbits and formation of chaotic regimes emerging in the damped-driven bilinear oscillator were performed by Thompson et al. [12], Shaw and Holmes [13]. In a later study, Natsiavas [14] considered the damped-driven response of bilinear (i.e. bilinear stiffness and bilinear damping parameters) oscillator. In the same study, the author managed to derive the exact solution for n-periodic orbits and analyzed their stability properties. Theoretical investigations of complex response regimes (i.e. sub- and super-harmonic resonances, chaotic motion) of resonantly driven, damped PWLO have been supported by experimental studies (see e.g. Shaw and Enrich [15, 16]). The vast majority of previous studies have focused on the response of bilinear oscillators to external loading, whereas their parametrically driven counterparts have received significantly less attention. Several theoretical works have analysed the response of parametrically forced bilinear oscillator. Series of two theoretical studies reported by Natsiavas et al [17] and Theodossiades and Natsiavas [18] have analyzed various types of periodic regimes exhibited by the gear pair backlash system which, under certain assumptions and simplifications can be modelled by parametrically and externally forced, bilinear oscillator. This was followed by another theoretical work by Marathe and Chatterjee [19] which considered the resonance response of parametrically driven, non-symmetric, bilinear Mathieu equation, which effectively models the aforementioned mechanical systems, studied by Natsiavas and co-workers [17, 18]. In the same study, authors have pursued an extensive computational study of instability regions emerging in the asymmetric bilinear Mathieu equation and revealed additional families of resonant tongues, which do not exist in the linear Mathieu equation. In the same study authors have provided the analytical justification for the realization of periodic solutions on transition curves separating the stable and unstable regions. Another theoretical study by Belovodsky [20], has considered the response of vibro-machine which contains the internal vibro-exciter and is mounted on linear elastic supports with soft elastic limiters. Starosvetsky et al [21, 22] have studied the piecewise linear single degree of freedom (SDOF) system analytically using action-angle variable and other approximate methods. At the same time, Kumar et al [23, 24] have studied transition regions of the bilinear coupled two-oscillators parametrically excited in the neighborhood of similar and non-similar nonlinear normal modes (NNMs).

Despite the extensive literature on bilinear oscillators and Mathieu-type equations, existing studies have largely focused either on symmetric parametric excitation or on numerical characterization of instability regions. In contrast, the present work extends existing asymmetric Hill formulations by incorporating simultaneous state-dependent stiffness, damping, and parametric excitation. The present model should be regarded as an idealized representation of asymmetric state-dependent dissipation and as a mathematically tractable prototype for analytical investigation. Closed-form transition curves are derived explicitly for primary $(1:1)$ and higher-order subharmonic resonances $(2:1$, $3:1$ and $4:1)$, revealing instability mechanisms and tongue interactions that do not arise in classical Mathieu or symmetric bilinear formulations. Importantly, the analysis is not restricted to an abstract lumped model: it is rigorously shown that the same asymmetric Hill equation governs the reduced-order dynamics of a base-excited cantilever beam with a breathing crack. This continuum–lumped equivalence provides a direct physical interpretation of the asymmetric excitation terms and enables the analytical instability boundaries to be used as predictive tools for parametric instability in cracked structural systems. The results therefore go beyond numerical observation, offering closed-form criteria with direct applicability to engineering structures exhibiting state-dependent nonlinearities.

The paper is organized as follows. In section 2, we discuss the lumped model for a bilinear oscillator with asymmetric parametric excitation. In section 3, the method of averaging procedures has been outlined in the context of the present problem. In section 4, we present the validation of the slow-flow model with numerical analysis for different resonance conditions. Further stability analysis and validation with numerical integration have been presented in section 5. In section 6, we present an engineering application of the proposed model.

Finally, we conclude our work in section 7.

2 Lumped model of a bilinear oscillator with piecewise linear parametric excitation

We consider a bilinear oscillator subjected to piecewise-defined stiffness, damping, and parametric excitation. The governing equation is

$$u_{tt} + \epsilon\lambda(u)u_t + K(u)u + \epsilon P(u)\left(\cos\Omega t\right) u = 0 \ , \tag{1}$$

where Ω is excitation frequency, $(\ )_t$ represent derivatives with respect to t and $\lambda(u)$, $K(u)$ and $P(u)$ are state-dependent damping coefficient, stiffness and amplitude of parametric excitation of the system and given as,

$$\begin{aligned} \lambda(u) =& \lambda_0, \qquad \text{for} \quad u < 0 \ , \\ =& \lambda_1, \qquad \text{for} \quad u \geq 0 \ , \end{aligned} \tag{2}$$

$$\begin{aligned} K(u) =& 1, \qquad \text{for} \quad u < 0 \ , \\ =& \delta^2, \qquad \text{for} \quad u \geq 0 \ , \end{aligned} \tag{3}$$

and

$$\begin{aligned} P(u) =& P_0, \qquad \text{for} \quad u < 0 \ , \\ =& P_1, \qquad \text{for} \quad u \geq 0 \ , \end{aligned} \tag{4}$$

We introduce excitation frequency as $\Omega = m\Omega_N - \epsilon\sigma$, Ω_N is bilinear natural frequency and defined as

$$\Omega_N = \frac{2\delta}{1+\delta} \ , \tag{5}$$

and σ is detuning parameter, Thus, Eq. (1) becomes,

$$u_{tt} + \epsilon\lambda_0 u_t + u + \epsilon P_0 \cos\big((m\Omega_N - \epsilon\sigma)t\big)\, u = 0 \qquad u < 0, \tag{6}$$

$$u_{tt} + \epsilon\lambda_1 u_t + \delta^2 u + \epsilon P_1 \cos\big((m\Omega_N - \epsilon\sigma)t\big)\, u = 0 \qquad u \geq 0, \tag{7}$$

To simplify the subsequent analysis, a new time scale is introduced as $m\Omega_N\tau = (m\Omega_N + \epsilon\sigma)t$, i.e., $\tau = \left(1 + \dfrac{\epsilon\sigma}{m\Omega_N}\right)t$. which yields time derivative as

$$\frac{d}{dt}(\,) = \left(1 + \frac{\epsilon\sigma}{m\Omega_N}\right)\frac{d}{d\tau}(\,)\,, \quad \text{and} \quad \frac{d^2}{dt^2}(\,) = \left(1 + \frac{\epsilon\sigma}{m\Omega_N}\right)^2\frac{d^2}{d\tau^2}(\,) \tag{8}$$

Using Eq. (8) the transformed form of Eqs. (6) and (7) are given as:

$$\left(1 + \frac{\epsilon\sigma}{m\Omega_N}\right)^2\frac{d^2u}{d\tau^2} + \epsilon\lambda_0\left(1 + \frac{\epsilon\sigma}{m\Omega_N}\right)\frac{du}{d\tau} + u + \epsilon P_0\cos(m\Omega_N\tau)u = 0 \qquad u < 0\,, \tag{9}$$

$$\left(1 + \frac{\epsilon\sigma}{m\Omega_N}\right)^2\frac{d^2u}{d\tau^2} + \epsilon\lambda_0\left(1 + \frac{\epsilon\sigma}{m\Omega_N}\right)\frac{du}{d\tau} + \delta^2 u + \epsilon P_0\cos(m\Omega_N\tau)u = 0 \qquad u \geq 0. \tag{10}$$

Further simplification of Eqs. (9) and (10) yields,

$$\frac{d^2u}{d\tau^2} + \epsilon\lambda_0\left(1 + \frac{\epsilon\sigma}{m\Omega_N}\right)^{-1}\frac{du}{d\tau} + \left(1 + \frac{\epsilon\sigma}{m\Omega_N}\right)^{-2}u + \epsilon P_0\left(1 + \frac{\epsilon\sigma}{m\Omega_N}\right)^{-2}\cos(m\Omega_N\tau)u = 0 \qquad u < 0\,, \tag{11}$$

$$\frac{d^2u}{d\tau^2} + \epsilon\lambda_0\left(1 + \frac{\epsilon\sigma}{m\Omega_N}\right)^{-1}\frac{du}{d\tau} + \delta^2\left(1 + \frac{\epsilon\sigma}{m\Omega_N}\right)^{-2}u + \epsilon P_0\left(1 + \frac{\epsilon\sigma}{m\Omega_N}\right)^{-2}\cos(m\Omega_N\tau)u = 0 \qquad u \geq 0\,, \tag{12}$$

Here, $\dfrac{\epsilon\sigma}{m\Omega_N}$ is much smaller than one, so we approximate the following expressions:

$$\left(1 + \frac{\epsilon\sigma}{m\Omega_N}\right)^{-2} \approx \left(1 - \frac{2\epsilon\sigma}{m\Omega_N}\right), \quad \text{and} \quad \left(1 + \frac{\epsilon\sigma}{m\Omega_N}\right)^{-1} \approx \left(1 - \frac{\epsilon\sigma}{m\Omega_N}\right)\,. \tag{13}$$

Finally, we simplify Eqs. (11) and (12) using relation given in Eq. (13) and retaining only terms upto the $\mathcal{O}(\epsilon)$ and neglecting other terms of order $\mathcal{O}(\epsilon^2)$ and higher. The simplified form of equations are

$$\ddot{u} + \epsilon\lambda_0\dot{u} + \left(1 - \frac{2\epsilon\sigma}{m\Omega_N}\right)u + \epsilon P_0\cos\left(m\Omega_N\tau\right)u = 0 \qquad u < 0, \tag{14}$$

$$\ddot{u} + \epsilon\lambda_1\dot{u} + \left(1 - \frac{2\epsilon\sigma}{m\Omega_N}\right)\delta^2 u + \epsilon P_1\cos\left(m\Omega_N\tau\right)u = 0 \qquad u \geq 0, \tag{15}$$

where overdots represent derivatives with respect to τ. These equations (Eqs. (14) and (15)) form the basis for the averaging procedure described in the next section. The list of system parameters along with their physical meaning and numerical range for the analysis is tabulated below.

Parameter	Physical meaning	Numerical values used
δ^2	Stiffness asymmetry parameter	$1-5$
$\lambda_0,\ \lambda_1$	State-dependent damping coefficients	$0-0.02$
$P_0,\ P_1$	Parametric excitation amplitudes in two states	$0-1$
σ	Detuning parameter	$-0.5-0.5$
m	Resonance order	$1-4$
Ω_N	Bilinear natural frequency	Defined by Eq. (5)
ϵ	Small perturbation parameter	0.1

3 Averaging method for bilinear oscillator

Before applying the method of averaging, it should be noted that the present bilinear oscillator belongs to the class of continuous piecewise-smooth systems. Although the stiffness, damping, and excitation coefficients switch according to the sign of the displacement, the displacement and velocity remain continuous across the switching instants. Consequently, the system does not exhibit sliding modes or set-valued dynamics characteristic of classical Filippov systems [25]. The non-smoothness is therefore restricted to abrupt changes in the system coefficients and may induce discontinuities only in higher-order derivatives. Under the assumptions of weak damping, weak parametric excitation, and small detuning, the response remains dominated by a slowly modulated oscillation. The averaging method is therefore employed to derive approximate slow-flow equations governing the evolution of the oscillation amplitude and phase. The resulting averaged equations should be interpreted as asymptotic approximations valid within the considered perturbation regime, and their accuracy is subsequently assessed through direct numerical simulations.

To derive slow evolution equations for amplitude and phase, we pose the solution for Eqs. (14) and (15) in piecewise form over one bilinear cycle. The solution is assumed in the following form,

$$u(\tau) =A(\tau)\sin\left(\omega_1 \mathrm{mod}(\tau+\phi(\tau),\mathrm{T})\right)\ ,\quad 0\le \mathrm{mod}(\tau+\phi,\mathrm{T})\le \frac{\pi}{\omega_1} \tag{16}$$

$$=A(\tau)\gamma\sin\Big(\omega_2 \mathrm{mod}(\tau+\phi(\tau),\mathrm{T})+\pi(1-\gamma^{-1})\Big)\ ,\quad \frac{\pi}{\omega_1}\le mod(\tau+\phi,T)\le T\ . \tag{17}$$

where $\gamma=\frac{\omega_1}{\omega_2}$ this parameter has been introduced to force continuity of the velocity). and T is the time period of the bilinear oscillators, $\omega_1=1$ and $\omega_2=\delta$. Bilinear frequency is defined as $\Omega_N=\dfrac{2\omega_1\omega_2}{\omega_1+\omega_2}$.

Introducing $\Psi = \tau + \phi$ and $\pi(1-\gamma^{-1}) = \rho$ and Eqs. (16) and (17) simplify to

$$u(\tau) = A(\tau)\sin\big(\omega_1 \mathrm{mod}(\Psi,\mathrm{T})\big)\ , \quad 0 \le \mathrm{mod}(\Psi,\mathrm{T}) \le \frac{\pi}{\omega_1} \tag{18}$$

$$= A(\tau)\gamma\sin\Big(\omega_2 \mathrm{mod}(\Psi,\mathrm{T}) + \pi(1-\gamma^{-1})\Big)\ , \quad \frac{\pi}{\omega_1} \le mod(\Psi,T) \le T\ . \tag{19}$$

The piecewise solutions Eqs. (18)-(19) are constructed to satisfy the continuity conditions

$$u(\tau)^- = u(\tau)^+ \quad \text{and} \quad \dot{u}(\tau)^- = \dot{u}(\tau)^+\ .$$

at every switching instant. Consequently, the trajectory remains continuous throughout one bilinear period while the acceleration undergoes finite jumps due to the abrupt change in the system coefficients. Next we substitute solutions (given in Eqs. (18)-(19)) into Eqs. (14)-(15) and deal each region separately.

Case: I $u < 0$ i.e., $0 \le \mathrm{mod}(\Psi,\mathrm{T}) \le \dfrac{\pi}{\omega_1}$

$$\dot{u} = \dot{A}\sin\big(\omega_1 \mathrm{mod}(\Psi,\mathrm{T})\big) + A\omega_1(1+\dot{\phi})\cos\big(\omega_1 \mathrm{mod}(\Psi,\mathrm{T})\big)\ , \tag{20}$$

Assuming that $\dot{u} = A\omega_1\cos\big(\omega_1 \mathrm{mod}(\Psi,\mathrm{T})\big)$, the corresponding compatibility condition becomes

$$\dot{A}\sin\big(\omega_1 \mathrm{mod}(\Psi,\mathrm{T})\big) + A\omega_1\dot{\phi}\cos\big(\omega_1 \mathrm{mod}(\Psi,\mathrm{T})\big) = 0\ . \tag{21}$$

Substituting the expressions of u and $\dot{u}$ in (14), we get

$$\begin{aligned}&\dot{A}\omega_1\cos\big(\omega_1 \mathrm{mod}(\Psi,\mathrm{T})\big) - A\omega_1^2\dot{\phi}\sin\big(\omega_1 \mathrm{mod}(\Psi,\mathrm{T})\big) + \epsilon\Big(\lambda_0 A\omega_1\cos\big(\omega_1 \mathrm{mod}(\Psi,\mathrm{T})\big)\\ &-\frac{2\sigma\omega_1^2 A}{m\Omega_N}\sin\big(\omega_1 \mathrm{mod}(\Psi,\mathrm{T})\big) + AP_0\cos(m\Omega_N(\Psi-\phi))\sin\big(\omega_1 \mathrm{mod}(\Psi,\mathrm{T})\big)\Big) = 0\ .\end{aligned} \tag{22}$$

Solving Eqs. (21) and (22) yields

$$\dot{A} = -\frac{\epsilon A}{2}\frac{\sin(2\omega_1\Psi)\left(P_0\cos(m\Omega_N(\Psi-\phi)) - \frac{2\sigma\omega_1^2}{m\Omega_N}\right)}{\omega_1} - \epsilon\lambda_0\cos^2(\omega_1\Psi)\ , \tag{23}$$

$$\dot{\phi} = \frac{\epsilon\sin^2(\omega_1\Psi)\left(P_0\cos(m\Omega_N(\Psi-\phi)) - \frac{2\sigma\omega_1^2}{m\Omega_N}\right)}{\omega_1^2} + \frac{\epsilon\lambda_0}{2\omega_1}\sin(2\omega_1\Psi)\ . \tag{24}$$

Case: II $u \ge 0$ **i.e.,** $\dfrac{\pi}{\omega_1} \le \mathrm{mod}(\Psi,\mathrm{T}) \le \mathrm{T}$

$$\dot{u} = \dot{A}\gamma\sin(\omega_2 \mathrm{mod}(\Psi,\mathrm{T}) + \rho) + \mathrm{A}\gamma\omega_2(1+\dot{\phi})\cos(\omega_2 \mathrm{mod}(\Psi,\mathrm{T}) + \rho); \tag{25}$$

Assume $\dot{u} = A\gamma\omega_2 \cos(\omega_2 \mathrm{mod}(\Psi, \mathrm{T}) + \rho)$. Thus compatibility condition (from Eq. (25))

$$\dot{A}\gamma \sin(\omega_2 \mathrm{mod}(\Psi, \mathrm{T}) + \rho) + \mathrm{A}\gamma\omega_2\dot{\phi}\cos(\omega_2 \mathrm{mod}(\Psi, \mathrm{T}) + \rho) = 0 \; . \tag{26}$$

and substituting the expression of u in Eq. (14)

$$\dot{A}\omega_2 \cos(\omega_2 \mathrm{mod}(\Psi, \mathrm{T}) + \rho) - \mathrm{A}\omega_2^2\dot{\phi}\sin(\omega_2 \mathrm{mod}(\Psi, \mathrm{T}) + \rho) + \epsilon\Bigg(\lambda_1 \mathrm{A}\omega_2 \cos(\omega_2 \mathrm{mod}(\Psi, \mathrm{T}) + \rho)$$
$$-\frac{2\sigma\omega_2^2 A}{m\Omega_N}\sin(\omega_2 \mathrm{mod}(\Psi, \mathrm{T}) + \rho) + \mathrm{AP}_1 \cos(\mathrm{m}\Omega_\mathrm{N}(\Psi - \phi))\sin(\omega_2 \mathrm{mod}(\Psi, \mathrm{T}) + \rho)\Bigg) = 0 \; . \tag{27}$$

Solving Eqs.‘(26) and (27), we get

$$\dot{A} = -\frac{\epsilon A}{2}\frac{\sin(2\omega_2\Psi + 2\rho)\left(P_1\cos(m\Omega_N(\Psi - \phi)) - \frac{2\sigma\omega_2^2}{m\Omega_N}\right)}{\omega_2} - \epsilon\lambda_1\cos^2(\omega_2\Psi + \rho) \; , \tag{28}$$

$$\dot{\phi} = \frac{\epsilon\sin^2(\omega_2\Psi + \rho)\left(P_1\cos(m\Omega_N(\Psi - \phi)) - \frac{2\sigma\omega_2^2}{m\Omega_N}\right)}{\omega_2^2} + \frac{\epsilon\lambda_1}{2\omega_2}\sin(2\omega_2\Psi + 2\rho) \; . \tag{29}$$

Using Eqs. (23)-(24) and Eqs. (28)-(29), the slow evolution of amplitude and phase is obtained by averaging over one cycle (through the first and the second states of motion)

$$\begin{aligned}\dot{A} =& \frac{1}{T}\int_0^{\frac{\pi}{\omega_1}}\left(-\frac{\epsilon A}{2}\frac{\sin(2\omega_1\Psi)\left(P_0\cos(\Omega_N(\Psi - \phi)) - \frac{2\sigma\omega_1^2}{m\Omega_N}\right)}{\omega_1} - \epsilon\lambda_0\cos^2(\omega_1\Psi)\right)d\Psi + \\ &\frac{1}{T}\int_{\frac{\pi}{\omega_1}}^{T}\left(-\frac{\epsilon A}{2}\frac{\sin(2\omega_2\Psi + 2\rho)\left(P_1\cos(m\Omega_N(\Psi - \phi)) - \frac{2\sigma\omega_2^2}{m\Omega_N}\right)}{\omega_2} - \epsilon\lambda_1\cos^2(\omega_2\Psi + \rho)\right)d\Psi \; .\end{aligned} \tag{30}$$

$$\begin{aligned}\dot{\phi} =& \frac{1}{T}\int_0^{\frac{\pi}{\omega_1}}\left(\frac{\epsilon\sin^2(\omega_1\Psi)\left(P_0\cos(\Omega_N(\Psi - \phi)) - \frac{2\sigma\omega_1^2}{m\Omega_N}\right)}{\omega_1^2} + \frac{\epsilon\lambda_0}{2\omega_1}\sin(2\omega_1\Psi)\right)d\Psi + \\ &\frac{1}{T}\int_{\frac{\pi}{\omega_1}}^{T}\left(\frac{\epsilon\sin^2(\omega_2\Psi + \rho)\left(P_1\cos(m\Omega_N(\Psi - \phi)) - \frac{2\sigma\omega_2^2}{m\Omega_N}\right)}{\omega_2^2} + \frac{\epsilon\lambda_1}{2\omega_2}\sin(2\omega_2\Psi + 2\rho)\right)d\Psi \; ..\end{aligned} \tag{31}$$

$$\dot{A} = -\epsilon A\left\{(\kappa_{11}P_0 + \kappa_{12}P_1)\sin(m\Omega_N\phi) + (\kappa_{13}P_0 + \kappa_{14}P_1)\cos(m\Omega_N\phi)\right\} - \epsilon A\left(\kappa_{15}\lambda_0 + \kappa_{16}\lambda_1\right) \; , \tag{32}$$

$$\dot{\phi} = -\epsilon\left\{(\kappa_{21}P_0 + \kappa_{22}P_1)\sin(m\Omega_N\phi) + (\kappa_{23}P_0 + \kappa_{24}P_1)\cos(m\Omega_N\phi)\right\} - \epsilon\kappa_{25}\sigma \tag{33}$$

Eqs. (32) and (33) are slow-flow equations and where $\kappa_{i,j}$ are constants and given below.

4 Validation of slow-flow model

The accuracy of the averaged equations derived in the previous section is assessed by comparing their predictions with direct numerical integration of the full bilinear system. Figure 1 illustrates the validation of the slow-flow model against direct numerical integration of the full nonlinear system. The comparison demonstrates close agreement, confirming the validity of the averaging method employed to derive the slow-flow equations. The results are presented for two resonance conditions, namely the primary resonance $(1:1)$ and the superharmonic resonances $(2:1$, $3:1$ and $4;1)$. For each resonance condition, two distinct sets of parameters are examined in the neighborhood of the transition curves to capture different dynamical behaviors: Bounded (stable) response: A parameter set corresponding to stable, bounded oscillations is chosen. Both the slow-flow predictions and the numerical simulations yield nearly identical trajectories, indicating that the reduced-order model captures the essential system dynamics. Unbounded (unstable) response: A parameter set corresponding to instability and unbounded growth of oscillations is examined. The slow-flow model also reproduces the numerical results closely, predicting the onset of instability and the qualitative features of the response.

The close correspondence across all resonance conditions (as shown in Fig. 1) confirms that the averaging procedure provides a reliable reduced-order representation of the bilinear system. These results justify the use of the slow-flow equations to derive analytical transition curves and stability boundaries, especially in practical engineering applications where computational efficiency is crucial in the following section.

Further, we consider a high stiffness asymmetry, i.e., $(1:\delta^2 = 1:5)$, to verify the slow-flow model (see Appendix B). It is again observed that, irrespective of the degree of stiffness asymmetry, the derived averaged slow-flow model shows good agreement with the numerical integration of the full model as shown in Fig. 9 in Appendix B. The presented results demonstrate that, as long as the amplitude of the parametric excitation and the detuning parameters are of $\mathcal{O}(\epsilon)$, the averaged slow-flow model remains in close agreement with the numerical solution of the full system, regardless of the stiffness asymmetry.

5 Stability Analysis

To obtain the transition curves, we set $\dot{A} = \dot{\phi} = 0$ in Eqs. (32) and (33)

$$-\epsilon A\left\{(\kappa_{11}P_0+\kappa_{12}P_1)\sin(m\Omega_N\phi)+(\kappa_{13}P_0+\kappa_{14}P_1)\cos(m\Omega_N\phi)\right\}-\epsilon A\left(\kappa_{15}\lambda_0+\kappa_{16}\lambda_1\right)=0\ , \tag{34}$$

$$-\epsilon\left\{(\kappa_{21}P_0+\kappa_{22}P_1)\sin(m\Omega_N\phi)+(\kappa_{23}P_0+\kappa_{24}P_1)\cos(m\Omega_N\phi)\right\}-\epsilon\kappa_{25}\sigma=0 \tag{35}$$

Eliminating $\cos(m\Omega_N\phi)$ and $\sin(m\Omega_N\phi)$ from Eqs. (34) and (35), we get

$$\begin{aligned}
&\left[(\kappa_{11}P_0+\kappa_{12}P_1)\kappa_{25}\sigma-(\kappa_{15}\lambda_0+\kappa_{16}\lambda_1)(\kappa_{21}P_0+\kappa_{22}P_1)\right]^2\\
&+\left[(\kappa_{13}P_0+\kappa_{14}P_1)\kappa_{25}\sigma-(\kappa_{15}\lambda_0+\kappa_{16}\lambda_1)(\kappa_{23}P_0+\kappa_{24}P_1)\right]^2\\
&=\left[(\kappa_{11}P_0+\kappa_{12}P_1)(\kappa_{23}P_0+\kappa_{24}P_1)-(\kappa_{13}P_0+\kappa_{14}P_1)(\kappa_{21}P_0+\kappa_{22}P_1)\right]^2\ .
\end{aligned} \tag{36}$$

The expression given in Eq. (36) is the implicit expression of the transition curve. The transition curve can be plotted in the plane of detuning parameter and excitation amplitude to present the instability boundaries for different resonance conditions. Figure. 2 through 5 present the instability diagram in the plane of detuning parameter σ and excitation amplitude P_0, for a given fixed value of P_1. These charts are generated using two approaches: (i) numerical simulation of the full model and (ii) the analytical expression given in Eq. (36) for $1:1$, $2:1$, $3:1$ and $4:1$ resonance conditions. Here red and green zones are for unstable and stable zones, respectively, and thick black solid lines represent the instability boundaries corresponding to the closed-form expression given in Eq. (36). We generated stability charts for two different sets of damping parameters by varying the damping (λ_2) associated with one state (i.e., $u(\tau)>0$), considering low damping (left panels) and high damping (right panels), while keeping the damping (λ_1) corresponding to the other state (i.e., $u(\tau)<0$) constant. The instability boundaries obtained using the two different approaches are in good agreement. To further validate the proposed formulation, instability charts were also generated numerically and compared with the closed-form expressions for a relatively larger stiffness asymmetry (i.e., $1:\delta^2=1:5$), as presented in Fig. 10 (Appendix B). Again, the instability boundaries predicted by the two approaches show good agreement. It is observed that, for small excitation amplitudes, the results obtained from the averaging method closely match those obtained from direct numerical integration of the full model. Furthermore, stability charts were also generated for larger excitation amplitudes (i.e., $P_0,\ P_1=\mathcal{O}(1)$) as shown in Fig. .11 (in Appendix C). In this case, the transition curves predicted by the averaged equations remain in good agreement with the stability boundaries obtained from the full model in Fig. 11 for three resonance conditions e.g., $1:1$, $2:1$, $3:1$. However, the corresponding slow-flow responses exhibit noticeable quantitative differences, although both approaches consistently predict the same qualitative behavior by correctly distinguishing between bounded and unbounded responses as shown in in Fig. 12 (in Appendix C).

We observe several noteworthy features of the system in the stability charts. For instance, in Fig. 2 (corresponding to the $1:1$ resonance condition), two instability tongues—one emerging from below and the other from above—approach each other. The gap between these two tongues is governed by the damping parameters. For nearly zero damping, both tongues meet at a fixed value of P_0 and at $\sigma = 0$ for a given resonance condition. In contrast, in Fig. 3 (for the $2:1$ resonance condition), there is only a single instability tongue that possesses a significant width at $P_0 = 0$ and in the neighborhood of $\sigma = 0$. This width gradually decreases to zero with increasing damping, as illustrated in Fig. 3b. Similarly, the instability charts for the $3:1$ resonance condition, shown in Figs. 4a and 4b, exhibit a similar qualitative trend to that of the $1:1$ case (as shown in Figs. 2a and 2b).

As we see in Fig. 6, for zero damping, there is a crossing point for a nonzero value of P_1. We established a general relation to find the crossing point (i.e., for a given value of P_1, shift (upward or downward) of instability tongue) as

$$P_0 = C_0 P_1 \ , \tag{37}$$

where C_0 is a constant for a given system parameter (δ) and resonance conditions ($m:1$) and given as $C_0 = \left(\dfrac{m^2\Omega_N^2 - 4\omega_1^2}{m^2\Omega_N^2 - 4\omega_2^2}\right)$, where and $\omega_1 = 1$, $\omega_2 = \delta$ and $\Omega_N = \dfrac{2\delta}{1+\delta}$. Equation. (37) shows that for a given system parameter and resonance condition, the crossing point varies linearly with P_1. The crossing point (i.e., value of P_0 at $\sigma = 0$) varies linearly with P_1 for the given system parameters (δ) and resonance condition ($m:1$) for zero damping case. The analytical developments presented in Sections 2–5 establish a general framework for bilinear oscillators with state-dependent stiffness, damping, and parametric excitation, formulated as an asymmetric Hill equation and validated through closed-form transition curves and numerical simulations. While these results are derived for an abstract lumped-parameter model, many practical structural systems exhibiting intermittent contact or stiffness switching can be mapped onto this formulation. In particular, beams with breathing cracks under base excitation naturally possess state-dependent stiffness and excitation amplitudes arising from crack opening–closing mechanisms. Motivated by this correspondence, Section 6 demonstrates how the governing continuum equations of a base-excited cantilever beam with a breathing crack, when reduced via modal projection, lead to a single-degree-of-freedom bilinear model that is mathematically equivalent to the asymmetric Hill equation studied earlier. This connection provides a rigorous physical interpretation of the lumped model parameters and confirms that the analytical instability boundaries derived in the preceding sections are directly applicable to continuum-based cracked-beam systems.

6 Continuum–Lumped Model Equivalence: A Base-Excited Cantilever Beam with a Breathing Crack

The analytical framework developed in the preceding sections addresses the stability of bilinear oscillators with state-dependent stiffness, damping, and parametric excitation, formulated in terms of an asymmetric Hill equation. In this section, we demonstrate that the same mathematical structure arises naturally from a physically motivated continuum system, namely a base-excited cantilever beam with a breathing crack. Starting from the governing partial differential equations of motion and employing a systematic modal reduction, we show that the resulting reduced-order model exhibits piecewise-defined stiffness and excitation parameters identical to those assumed in the lumped formulation. This establishes a rigorous equivalence between the abstract asymmetric Hill model and the dynamics of cracked beam structures, thereby providing a direct physical interpretation of the analytical results and enabling their application to practical structural instability problems.

Cantilever beams with cracks arise in a wide range of engineering applications, including aerospace structures, wind turbine blades, and civil infrastructure. The presence of a crack significantly alters the dynamic response drastically, particularly when the crack exhibits breathing behaviour such as opening and closing during vibration as shown in Fig. 8. Such systems possess state-dependent stiffness and, consequently, exhibit bilinear characteristics. Several studies are available in the literature addressing cracks or any stiffness singularities present in the beam structures. Chondros et al [26] have studied vibration-based methods to identify the presence of cracks and wended joints. Rizos et al [27] have used vibration modes of the beam to identify the location and intensity of the present cracks. Shufrin et al [28] have derived the dispersion relation and mode shape for the cantilever beam with arbitrary number of cracks. Later, Cadami et al [29] derived the close form for the mode shape of the beam with open cracks by approximating cracks as singularities in the stiffness. Maiti et al [30] have presented the detail dynamic behavior of the cantilever beam with presence of open crack. Recently, Avramov et al [31] have studied the nonlinear normal mode and bifurcation study of the beam with breathing cracks incorporating geometric nonlinearities. This section develops a reduced-order model for a cantilever beam with a breathing crack and demonstrates its equivalence to the asymmetric Hill-type formulation introduced earlier.

6.1 Problem Formulation: Initial-boundary-value problem

Consider a cantilever beam of length L containing a single breathing crack located along axial direction is considered as $x = x_0$ such that $0 < x_0 < L$. When the crack is closed, the beam behaves as an intact structure; when it is open, the crack introduces localized flexibility. Following the standard practice (mentioned by [27, 28, 32]), the beam with a single open crack is modeled by inserting a massless rotational spring at the crack position. Although the present formulation considers a single crack, it can be readily generalized to multiple cracks. For a single crack, it is possible to divide the entire beam into two beams connected by massless springs representing a crack at $x = x_0$. Let the transverse displacement be denoted by $\hat{u}_1(x,t)$ in the interval $0 \geq x \leq x_0$ (i.e., 1st part of the beam) and $\hat{u}_2(x,t)$ in the interval $x_0 < x \leq L$ (i.e., 2nd part of the beam). The generalized displacement of the whole beam $\hat{u}(x,\hat{t})$ is defined as

$$\hat{u}(x,\hat{t}) = \hat{u}_1(x,\hat{t}) + \Big(\hat{u}_2(x,\hat{t}) - \hat{u}_1(x,\hat{t})\Big)\,\mathcal{H}(x-x_0) = \hat{u}_1(x,\hat{t}) + \Delta\hat{u}(x,\hat{t})\mathcal{H}(x-x_0)\;, \tag{38}$$

where $\Delta\hat{u}(x,\hat{t}) = \hat{u}_2(x,\hat{t}) - \hat{u}_1(x,\hat{t})$ and $\mathcal{H}(x-x_0)$ is heaviside function. The imposing boundary conditions at the crack

$$\hat{u}_1(x_0,\hat{t}) = \hat{u}_2(x_0,\hat{t}), \quad \text{i.e.,} \quad \Delta\hat{u}(x_0,\hat{t}) = 0\;, \tag{39a}$$

$$\hat{u}_1^{''}(x_0,\hat{t}) = \hat{u}_2^{''}(x_0,\hat{t}), \quad \text{i.e.,} \quad \Delta\hat{u}^{''}(x_0,\hat{t}) = 0\;, \tag{39b}$$

$$\hat{u}_1^{'''}(x_0,\hat{t}) = \hat{u}_2^{'''}(x_2,\hat{t}), \quad \text{i.e.,} \quad \Delta\hat{u}^{'''}(x_0,\hat{t}) = 0\;, \tag{39c}$$

$$\hat{u}_2^{'}(x_j,\hat{t}) - \hat{u}_1^{'}(x_0,\hat{t}) = \Delta\hat{u}^{'}(x_0,t) = \kappa = \hat{c}_1\hat{u}^{''}(x_0,\hat{t})\;, \tag{39d}$$

where $\hat{c}_1$ is the rotational stiffness of the spring and it is a function of the crack depth (a_j) and beam depth (h). The expression of $\hat{c}_1$ [27] is

$$\hat{c}_1 = 5.346 h f(\beta), \tag{40}$$

where $\beta_j = a_j/h$ and

$$f(\beta) = 1.8624\beta^2 - 3.95\beta^3 + 16.375\beta^4 - 37.226\beta^5 + 76.81\beta^6 - 126.9\beta^7 + 172\beta^8 - 143.97\beta^9 + 66.56\beta^{10}\;. \tag{41}$$

Derivatives of Eq. (38) with respect to x in generalized sense and imposing boundary conditions (given in Eqs. (39a)-(39d)) on cracks lead to

$$\tilde{\hat{u}}^{'}(x,\hat{t}) = \hat{u}_1^{'}(x,\hat{t}) + \Delta\hat{u}^{'}(x,\hat{t})\mathcal{H}(x-x_0) \tag{42a}$$

$$\tilde{\hat{u}}^{''}(x,\hat{t}) = \hat{u}_1^{''}(x,\hat{t}) + \Delta\hat{u}^{''}(x,\hat{t})\mathcal{H}(x-x_0) + \Delta\hat{u}^{'}(x_0,\hat{t})\delta(x-x_0) \tag{42b}$$

$$\tilde{\hat{u}}^{'''}(x,\hat{t}) = \hat{u}_1^{'''}(x,\hat{t}) + \Delta\hat{u}^{'''}(x,\hat{t})\mathcal{H}(x-x_0) + \Delta\hat{u}^{'}(x_0,\hat{t})\delta^{'}(x-x_0) \tag{42c}$$

$$\tilde{\hat{u}}^{iv}(x,\hat{t}) = \hat{u}_1^{iv}(x,\hat{t}) + \Delta\hat{u}^{iv}(x,\hat{t})\mathcal{H}(x-x_0) + \Delta\hat{u}^{'}(x_0,\hat{t})\delta^{''}(x-x_0) \tag{42d}$$

where $\tilde{\hat{u}}^{'}$, $\tilde{\hat{u}}^{''}$, $\tilde{\hat{u}}^{'''}$, $\tilde{\hat{u}}^{iv}$ are first, second, third and fourth derivatives of $\hat{u}(x,\hat{t})$ with respect to x, respectively in the generalized sense and $\delta(x-x_0)$ is Dirac delta function.

Equations of motion for each segment beam with transverse displacement $\hat{u}_1(x,\hat{t})$, $\hat{u}_2(x,\hat{t})$, respectively under base excitation [33] are

$$EI\hat{u}_1^{iv}(x,\hat{t}) + m\ddot{\hat{u}}_1(x,\hat{t}) - m\left(\hat{u}_1^{''}(x,\hat{t})(x-L) + \hat{u}_1^{'}(x,\hat{t})\right)(\hat{f}\hat{\Omega}^2\cos\hat{\Omega}\hat{t} + g) = 0,\ x_1 \le x < x_j, \tag{43a}$$

$$EI\hat{u}_2^{iv}(x,\hat{t}) + m\ddot{\hat{u}}_2(x,\hat{t}) - m\left(\hat{u}_2^{''}(x,\hat{t})(x-L) + \hat{u}_2^{'}(x,\hat{t})\right)(\hat{f}\hat{\Omega}^2\cos\hat{\Omega}\hat{t} + g) = 0,\ x_1 < x \le x_2, \tag{43b}$$

where E is the Young's modulus, I is the moment of inertia of the cross-section, m is the mass per unit length and $\hat{f}$ is amplitude of excitation , $\hat{\Omega}$ is frequency of excitation and g is acceleration due to gravity . Combining Eqs. (43a) and (43b) and we get a single equation which represent whole beam

$$\begin{aligned} EI\hat{u}_1^{iv}(x,\hat{t}) + m\ddot{\hat{u}}_1(x,\hat{t}) - m\left(\hat{u}_1^{''}(x,\hat{t})(x-L) + \hat{u}_1^{'}(x,\hat{t})\right)(\hat{f}\hat{\Omega}^2\cos\hat{\Omega}\hat{t} + g) + \Big[\Big\{EI\hat{u}_2^{iv}(x,\hat{t}) + m\ddot{\hat{u}}_2(x,\hat{t}) \\ - m\left(\hat{u}_2^{''}(x,\hat{t})(x-L) + \hat{u}_2^{'}(x,\hat{t})\right)(\hat{f}\hat{\Omega}^2\cos\hat{\Omega}\hat{t} + g)\Big\} - \Big\{EI\hat{u}_1^{iv}(x,\hat{t}) + m\ddot{\hat{u}}_1(x,\hat{t}) \\ - m\left(\hat{u}_1^{''}(x,\hat{t})(x-L) + \hat{u}_1^{'}(x,\hat{t})\right)(\hat{f}\hat{\Omega}^2\cos\hat{\Omega}\hat{t} + g)\Big\}\Big]\mathcal{H}(x-x_0) = 0\ . \end{aligned} \tag{44}$$

Rearranging Eq. (44) yields,

$$\begin{aligned} EI\hat{u}_1^{iv}(x,\hat{t}) + m\ddot{\hat{u}}_1(x,\hat{t}) - m\left(\hat{u}_1^{''}(x,\hat{t})(x-L) + \hat{u}_1^{'}(x,\hat{t})\right)(\hat{f}\hat{\Omega}^2\cos\hat{\Omega}\hat{t} + g) + \Big[EI\Delta\hat{u}^{iv}(x,\hat{t}) + m\Delta\ddot{\hat{u}}(x,\hat{t}) \\ - m\left(\Delta\hat{u}^{''}(x,\hat{t})(x-L) + \Delta\hat{u}^{'}(x,\hat{t})\right)(\hat{f}\hat{\Omega}^2\cos\hat{\Omega}\hat{t} + g)\Big]\mathcal{H}(x-x_0) = 0\ . \end{aligned} \tag{45}$$

Solving Eq. (46) for $EI\hat{u}_1^{iv}(x,t)$

$$\begin{aligned} EI\hat{u}_1^{iv}(x,\hat{t}) =& m(x-L)\left[\hat{u}_1^{''}(x,\hat{t}) + \Delta\hat{u}^{''}(x,\hat{t})\mathcal{H}(x-x_0)\right](\hat{f}\hat{\Omega}^2\cos\hat{\Omega}\hat{t} + g) + m\Big[\hat{u}_1^{'}(x,\hat{t}) \\ &+ \Delta\hat{u}^{'}(x,\hat{t})\mathcal{H}(x-x_0)\Big](\hat{f}\hat{\Omega}^2\cos\hat{\Omega}\hat{t} + g) - m\left(\ddot{\hat{u}}_1(x,\hat{t}) + m\Delta\ddot{\hat{u}}(x,\hat{t})\mathcal{H}(x-x_0)\right) \\ &+ EI\Delta\hat{u}^{iv}(x,\hat{t})\mathcal{H}(x-x_0)\ . \end{aligned} \tag{46}$$

Using Eqs. (42a) and (42b), rewrite Eq. (46) becomes

$$
\begin{aligned}
EI\hat{u}_1^{iv}(x,\hat{t}) =& m(x-L)\left[\tilde{\hat{u}}^{''}(x,\hat{t}) - \Delta\hat{u}^{'}(x_0,\hat{t})\delta(x-x_0)\right](\hat{f}\hat{\Omega}^2\cos\hat{\Omega}\hat{t}+g) + m\tilde{\hat{u}}^{'}(\hat{f}\hat{\Omega}^2\cos\hat{\Omega}\hat{t}+g) \\
&- m\ddot{\tilde{\hat{u}}}(x,\hat{t}) + EI\Delta\hat{u}^{iv}(x,\hat{t})\mathcal{H}(x-x_0)\;. \qquad (47)
\end{aligned}
$$

Multiplying Eq. (42d) by EI and substituting the expression of $EI\hat{u}_1^{iv}(x,\hat{t})$ (from Eq. (47)) yield,

$$
\begin{aligned}
EI\tilde{\hat{u}}^{iv}(x,\hat{t}) =& m(x-L)\left[\tilde{\hat{u}}^{''}(x,\hat{t}) - \Delta\hat{u}^{'}(x_0,\hat{t})\delta(x-x_0)\right](\hat{f}\hat{\Omega}^2\cos\hat{\Omega}\hat{t}+g) + m\tilde{\hat{u}}^{'}(\hat{f}\hat{\Omega}^2\cos\hat{\Omega}\hat{t}+g) \\
&- m\ddot{\tilde{\hat{u}}}(x,\hat{t}) + EI\Delta\hat{u}^{'}(x_0,\hat{t})\delta^{''}(x-x_0)\;. \qquad (48)
\end{aligned}
$$

Using Eq. (42d) in Eq. (48),

$$
\begin{aligned}
&EI\left[\tilde{\hat{u}}^{iv}(x,\hat{t}) - \hat{c}_1\hat{u}^{''}(x_0,\hat{t})\delta^{''}(x-x_0)\right] + m\ddot{\tilde{\hat{u}}}(x,\hat{t}) \\
&\quad = m(x-L)\left[\tilde{\hat{u}}^{''}(x,\hat{t}) - \hat{c}_1\hat{u}^{''}(x_0,\hat{t})\delta(x-x_0)\right](\hat{f}\hat{\Omega}^2\cos\hat{\Omega}\hat{t}+g) + m\tilde{\hat{u}}^{'}(x,\hat{t})\left(\hat{f}\hat{\Omega}^2\cos\hat{\Omega}\hat{t}+g\right)\;. \qquad (49)
\end{aligned}
$$

Adding phenomenological linear viscous damping term $2\hat{C}\dot{\hat{u}}(x,\hat{t})$ to the Eq. (49)

$$
\begin{aligned}
&EI\left[\tilde{\hat{u}}^{iv}(x,\hat{t}) - \hat{c}_1\hat{u}^{''}(x_0,\hat{t})\delta^{''}(x-x_0)\right] + m\ddot{\tilde{\hat{u}}}(x,\hat{t}) + 2\hat{C}\dot{\tilde{\hat{u}}}(x,\hat{t}) \\
&\quad = m(x-L)\left[\tilde{\hat{u}}^{''}(x,\hat{t}) - \hat{c}_1\hat{u}^{''}(x_0,\hat{t})\delta(x-x_0)\right](\hat{f}\hat{\Omega}^2\cos\hat{\Omega}\hat{t}+g) + m\tilde{\hat{u}}^{'}(x,\hat{t})\left(\hat{f}\hat{\Omega}^2\cos\hat{\Omega}\hat{t}+g\right)\;. \qquad (50)
\end{aligned}
$$

where $\hat{C}$ is coefficient of the linear viscous damping. Equation. (50) present a complete equation of motion for beams with multiple cracks under base excitation.

We rescale the dimensional equation of motion (in Eq. (50)) by the following length and time scales $\xi,\ t,\ u$,

$$
x = \xi L\;, \quad \hat{t} = \frac{t}{\omega_s}, \quad \hat{u} = uh\;, \qquad (51)
$$

where $\omega_s^2 = EI/mL^4$, h is the height of the beam cross-section and L is the length of the beam. Using length and time scale given in Eq. (51), we non-dimesionalize Eq. (50) get the non-dimensionalized equation of motion is

$$
\begin{aligned}
&\ddot{\tilde{u}}(\xi,t) + 2\delta\dot{\tilde{u}} + \left[\tilde{u}^{iv}(\xi,t) - c_1 u^{''}(\xi_0,t)\delta^{''}(\xi-\xi_0)\right] \\
&\quad = (\xi-1)\left[\tilde{u}^{''}(\xi,t) - c_1 u^{''}(\xi_0,t)\delta(\xi-\xi_0)\right](f_1\Omega^2\cos\Omega t + f_2) + \tilde{u}^{'}(\xi,t)(f_1\Omega^2\cos\Omega t + f_2)\;. \qquad (52)
\end{aligned}
$$

where primes ($'$) and dots ($\dot{}$) represent differentiation with respect to ξ and t respectively.

The non-dimensional parameters are

$$
c_1 = \frac{\hat{c}_1}{L}, \quad \delta = \frac{\hat{C}}{m\omega_s}, \quad f_1 = \frac{\hat{f}}{L}\;, \quad f_2 = \frac{g}{L\omega_s^2}\;, \quad \Omega = \frac{\hat{\Omega}}{\omega_s}\;. \qquad (53)
$$

We approximate $u(\xi, t)$ with single mode approximation as

$$u(\xi, t) = \phi(\xi) q(t) \ , \tag{54}$$

where $\phi(\xi)$ is the shape function and $q(t)$ is the corresponding generalized coordinate for the first mode. The expression of the shape function $\phi(\xi)$ for single breathing crack is given [8]

$$\begin{aligned} \phi_i(\xi) = b\phi_i^1(\xi) + (1-b)\phi_i^0(\xi) \ , \quad & b = 1 \quad \text{when crack is open} \\ & b = 0 \quad \text{when crack is closed} \end{aligned} \tag{55}$$

where ϕ_i^1 and ϕ_i^0 are shape functions of the cantilever beam when crack is open and closed, respectively (see Fig. 8). We assume that the mode shape for the open-crack state corresponds to that of the beam with an open crack, while the mode shape for the closed-crack state corresponds to that of the intact beam. The mdoe shape of the beam with open creak is gievn in Appendix D. Substituting the expression of $u(\xi, t)$ (from Eq. (55)) in Eq. (52) yields

$$\begin{aligned} &\ddot{q}_i(t)\phi_i(\xi) + 2\delta\dot{q}_i(t)\phi_i(\xi) + q_i(t)\left[\phi_i^{iv}(\xi) - c_1\phi_i^{''}(\xi_1)\delta^{''}(\xi-\xi_1)\right] \\ &+ q_i(t)(\xi-1)\left[\phi_i^{''}(\xi) - c_1\phi_i^{''}(\xi_1)\delta(\xi-\xi_1)\right](f_1\Omega^2\cos\Omega t + f_2) + q_i(t)\phi_i^{'}(\xi)(f_1\Omega^2\cos\Omega t + f_2) = 0 \ . \end{aligned} \tag{56}$$

where ($'$) and ($\dot{}$) represent differentiation with respect to ξ and t respectively. Multiplying each term of the Eq. (56) with $\phi_j(\xi)$ and integrate the outcome over the domain $\xi \in [0,\ 1]$ using the orthogonality condition $\int_0^1 \phi_i\phi_j d\xi = \delta_{ij}$.

$$\mathcal{M}_{ij}\ddot{q}_j(t) + \mathcal{C}_{ij}\dot{q}_j(t) + \mathcal{K}_{ij}q_j(t) = 0 \ , \tag{57}$$

where

$$\mathcal{M}_{ij} = \int_0^1 \phi_i\phi_j d\xi \ , \tag{58}$$

$$\mathcal{C}_{ij} = \int_0^1 \phi_i\phi_j d\xi \ , \tag{59}$$

$$\mathcal{K}_{ij} = \lambda_i^4 \int_0^1 \phi_i\phi_j d\xi + (f_1\cos\Omega t - f_2)\int_0^1 \left[\phi_i^{''}(\xi)(\xi-1) + \phi_i^{'}(\xi)\right]\phi_j(\xi)d\xi \ , \tag{60}$$

Similarly, integrals involve in second term of Eq. (60) can be simplified using integration by part and appropriate boundary conditions of the cantilever beam,

$$\begin{aligned} \int_0^1 \left[\phi_i^{''}(\xi)(\xi-1) + \phi_i^{'}(\xi)\right]\phi_j(\xi)d\xi = \xi\phi_i^{'}(\xi)\phi_j(\xi)\Big|_0^1 - \int_0^1 \phi_i^{'}(\xi)\phi_j(\xi)d\xi - \int_0^1 \xi\phi_i^{'}(\xi)\phi_j^{'}(\xi)d\xi \\ - \phi_i^{'}(\xi)\phi_j(\xi)\Big|_0^1 + \int_0^1 \phi_i^{'}(\xi)\phi_j^{'}(\xi)d\xi + \int_0^1 \phi_i^{'}(\xi)\phi_j(\xi)d\xi \ . \end{aligned} \tag{61}$$

Using boundary conditions of the cantilever beam Eq. (61) becomes,

$$\int_0^1 \left[\phi_i^{''}(\xi)(\xi-1)+\phi_i^{'}(\xi)\right]\phi_j(\xi)d\xi = \int_0^1 \phi_i^{'}(\xi)\phi_j^{'}(\xi)(1-\xi)d\xi\ . \tag{62}$$

Using Eqs. (61) and (62), the expression of the element of stiffness matrix given in Eqs. (60) modified as

$$\mathcal{K}_{ij} = \lambda_i^4 \int_0^1 \phi_i(\xi)\phi_j(\xi)d\xi + (f_1\cos\Omega t - f_2)\int_0^1 \phi_i^{'}(\xi)\phi_j^{'}(\xi)(1-\xi)d\xi\ . \tag{63}$$

Elements of the matrices $\mathcal{K}_{ij}$, $\mathcal{M}_{ij}$ and $\mathcal{C}_{ij}$ contain the integrals $\int_0^1 \phi_i(\xi)\phi_j(\xi)d\xi$ and $\int_0^1 \phi_i^{'}(\xi)\phi_j^{'}(\xi)(1-\xi)d\xi$, which are calculated as

$$\begin{aligned}\int_0^1 \phi_i(\xi)\phi_j(\xi)d\xi &= \int_0^1 \phi_i^0(\xi)\phi_j^0(\xi)d\xi;\ \ G(\xi_1,q)>0\ ,\\ &= \int_0^1 \phi_i^1(\xi)\phi_j^1(\xi)d\xi;\ \ G(\xi_1,q)<0\ ,\end{aligned} \tag{64}$$

and similarly,

$$\begin{aligned}\int_0^1 \phi_i^{'}(\xi)\phi_j^{'}(\xi)(1-\xi)d\xi &= \int_0^1 \phi_i^{0^{'}}(\xi)\phi_j^{0^{'}}(\xi)(1-\xi)d\xi; \qquad G(\xi_1,q)>0\ ,\\ &= \int_0^1 \phi_i^{1^{'}}(\xi)\phi_j^{1^{'}}(\xi)(1-\xi)d\xi; \qquad G(\xi_1,q)<0\ ,\end{aligned} \tag{65}$$

$i=1,\cdots,N$ and $j=1,\cdots,N$,

where

$$G(\xi,q)=\sum_{i=1}^{N}\frac{d^2}{d\xi^2}\phi_i^0(\xi)q_i(t)\ .$$

The integrals $\int_0^1 \phi_i\phi_j d\xi$ depend on the conditions of crack opening and closing. The crack opening and closing are described by the linear constraint $G(\xi_1,q)$.

The eigenmode satisfy the orthogonality condition

$$\int_0^1 \phi_i^b(\xi)\phi_j^b(\xi)d\xi = \pi_i^b\delta_{ij}, \qquad b=0,\ 1. \tag{66}$$

where δ_{ij} is called Kronecker delta. The values of the parameters π_i^b are calculated from the integral in Eq. (66). The dynamical modal system

$$M_{ij}\ddot{q}_j(t)+C_{ij}\dot{q}_j(t)+K_{ij}q_j(t)=0\ . \tag{67}$$

When crack is closed (i.e., $G(\xi_1, q) > 0$)

$$M_{ij}^0 = \int_0^1 \phi_i^0 \phi_j^0 d\xi \ , \tag{68a}$$

$$C_{ij}^0 = \int_0^1 \phi_i^0 \phi_j^0 d\xi \ , \tag{68b}$$

$$K_{ij}^0 = {\lambda_i^0}^4 \int_0^1 \phi_i^0(\xi)\phi_j^0(\xi) d\xi + (f_1 \cos\Omega t - f_2) \int_0^1 {\phi_i^0}'(\xi){\phi_j^0}'(\xi)(1-\xi) d\xi; , \tag{68c}$$

here λ_i^0 is calculated using relations in Eqs. (78) and (78).

When crack is opened (i.e., $G(\xi_1, q) < 0$)

$$M_{ij}^1 = \int_0^1 \phi_i^1 \phi_j^1 d\xi \ , \tag{69a}$$

$$C_{ij}^1 = \int_0^1 \phi_i^1 \phi_j^1 d\xi \ , \tag{69b}$$

$$K_{ij}^1 = {\lambda_i^1}^4 \int_0^1 \phi_i(\xi)\phi_j(\xi) d\xi + (f_1 \cos\Omega t - f_2) \int_0^1 {\phi_i^1}'(\xi){\phi_j^1}'(\xi)(1-\xi) d\xi; , \tag{69c}$$

here λ_i^1 is calculated using characteristics equation corresponding to the state of open crack.

6.2 Single mode approximation

In this section, we simplify the dynamical system for the cantilever beam with breathing crack using single mode approximation i.e., $N = 1$. We substitute $i = j = 1$ in Eq. (67) and get

$$M_{11}\ddot{q}_1(t) + C_{11}\dot{q}_1(t) + K_{11}q_1(t) = 0 \ . \tag{70}$$

and $G(\xi_1, q) = \frac{d^2}{d\xi^2}\phi_1^0(\xi_1) q_1(t)$. For a given location of the crack $\frac{d^2}{d\xi^2}\phi_1^0(\xi_1)$ is fixed. The sign of G will be decided solely by the sign of temporal coordinate $q_1(t)$. Assume the sign of $\frac{d^2}{d\xi^2}\phi_1^0(\xi_1)$ is positive for a given crack position. Then values of all coefficients (in Eq. (70)) will be decied by based on the sign of $q_1(t)$ at any instant. When crack is closed (i.e., $q_1 > 0$)

$$M_{11}^0 = \int_0^1 \phi_1^0 \phi_1^0 d\xi \ , \tag{71a}$$

$$C_{ij}^0 = \int_0^1 \phi_1^0 \phi_1^0 d\xi \ , \tag{71b}$$

$$K_{ij}^0 = {\lambda_1^0}^4 \int_0^1 \phi_1^0(\xi)\phi_1^0(\xi) d\xi + (f_1 \cos\Omega t - f_2) \int_0^1 {\phi_1^0}'(\xi){\phi_1^0}'(\xi)(1-\xi) d\xi; , \tag{71c}$$

here λ_i^0 is calculated using relations in Eqs. (78) and (78).

When crack is opened (i.e., $G(\xi_1, q) < 0$)

$$M_{11}^1 = \int_0^1 \phi_1^1 \phi_1^1 d\xi \ , \tag{72a}$$

$$C_{11}^1 = \int_0^1 \phi_1^1 \phi_1^1 d\xi \ , \tag{72b}$$

$$K_{11}^1 = {\lambda_1^1}^4 \int_0^1 \phi_1(\xi)\phi_1(\xi)d\xi + (f_1 \cos\Omega t - f_2) \int_0^1 {\phi_1^1}'(\xi){\phi_1^1}'(\xi)(1-\xi)d\xi; , \tag{72c}$$

We can further simplify Eq. (70) (assume gravity has negligible effect i.e, $f_2 = 0$) aligned with Eq. (1) as

$$\ddot{q}_1 + 2c\dot{q}_1 + K(q_1)q_1 + \epsilon P(q_1)\cos(\Omega t)q_1 = 0 \ , \tag{73}$$

where

$$\begin{aligned} K(q_1) =& {\lambda_1^1}^4 \int_0^1 \phi_1(\xi)\phi_1(\xi)d\xi, \qquad \text{for} \quad q_1 < 0 \ , \\ =& {\lambda_1^0}^4 \int_0^1 \phi_1^0(\xi)\phi_1^0(\xi)d\xi, \qquad \text{for} \quad q_1 \geq 0 \ , \end{aligned} \tag{74}$$

and

$$\begin{aligned} P(q_1) =& f_1 \int_0^1 {\phi_1^1}'(\xi){\phi_1^1}'(\xi)(1-\xi)d\xi, \qquad \text{for} \quad q_1 < 0 \ , \\ =& f_1 \int_0^1 {\phi_1^0}'(\xi){\phi_1^0}'(\xi)(1-\xi)d\xi, \qquad \text{for} \quad q_1 \geq 0 \ , \end{aligned} \tag{75}$$

Thus, Eq. (73) represents the reduced-order model for the cantilever beam with a breathing crack under base excitation which includes a state dependent variation in both stiffness and parametric excitation and it exhibits the same mathematical structure as the asymmetric Hill equation with asymmetric excitation. The presence of a breathing crack causes the beam to alternate between open- and closed-crack states, giving rise to a bilinear stiffness profile and a modulated excitation amplitude. The reduced single-mode formulation captures this state-dependent switching and naturally leads to an asymmetric Hill-type equation. This establishes a clear correspondence between the analytical developments presented earlier and the dynamics of cracked beams, enabling the closed-form transition curves to be employed as predictive tools for assessing parametric instability in practical structural applications.

7 Concluding Remarks

This work has presented an analytical framework for the stability analysis of bilinear oscillators with simultaneously state-dependent stiffness, damping, and parametric excitation, formulated as an asymmetric Hill equation. Unlike previous asymmetric Mathieu/Hill formulations, the present model incorporates asymmetry in all three system parameters and provides explicit slow-flow equations together with closed-form expressions for the transition curves corresponding to the primary and higher-order resonance conditions.

The method of averaging was applied to derive the slow-flow equations for this continuous piecewise-smooth system. Although the governing equations contain discontinuous coefficients, the displacement and velocity remain continuous across the switching instants, making the averaging procedure applicable within the weak perturbation regime. Extensive comparisons with direct numerical integration demonstrate good agreement for primary $(1:1)$ and subharmonic $(2:1,\ 3:1,\ 4:1)$ resonances. The proposed analytical framework accurately predicts instability boundaries over different stiffness asymmetries and damping configurations. Furthermore, even for larger excitation amplitudes, where the perturbation assumptions are formally relaxed, the analytical transition curves continue to predict the instability boundaries with good accuracy, although the slow-flow responses exhibit quantitative differences for large amplitudes of excitation (i.e., $P_1 = P_0 = \mathcal{O}(1)$) while preserving the correct qualitative distinction between bounded and unbounded motions.

The developed stability analysis reveals several characteristic features of asymmetric Hill equations, including the evolution and interaction of instability tongues, the influence of damping asymmetry on tongue separation, and the existence of a simple analytical relation governing the crossing points of instability boundaries (for zero damping). These results provide direct physical insight into the mechanisms controlling parametric instability in systems with state-dependent properties.

Finally, the study establishes a rigorous equivalence between the proposed asymmetric Hill formulation and the reduced-order dynamics of a base-excited cantilever beam with a breathing crack. The continuum-to-lumped reduction demonstrates that breathing-crack structures naturally exhibit state-dependent stiffness and excitation, leading to the same piecewise mathematical model developed in this work. Consequently, the derived closed-form transition curves provide an efficient analytical tool for predicting parametric instability in practical engineering systems exhibiting stiffness switching, including cracked beams, rotating machinery, and other structures with state-dependent nonlinearities.

The proposed framework provides a foundation for future studies on more complex piecewise-smooth systems involving multiple stiffness discontinuities, multi-mode interactions, geometric nonlinearities, and experimental validation.

Appendix A: Expression of κ_{ij}

$$\kappa_{11} = \frac{\Omega_N \left(4\omega_2^2 - m^2\Omega_N^2\right)\left(1 - \cos\left(\frac{m\pi\Omega_N}{\omega_1}\right)\right)}{2\pi\left(m^4\Omega_N^4 - 4m^2\Omega_N^2(\omega_1^2+\omega_2^2) + 16\omega_1^2\omega_2^2\right)} ,$$

$$\kappa_{12} = -\frac{\Omega_N \left(4\omega_1^2 - m^2\Omega_N^2\right)\left(1 - \cos\left(\frac{m\pi\Omega_N}{\omega_1}\right)\right)}{2\pi\left(m^4\Omega_N^4 - 4m^2\Omega_N^2(\omega_1^2+\omega_2^2) + 16\omega_1^2\omega_2^2\right)}$$

$$\kappa_{13} = -\frac{\Omega_N \left(4\omega_2^2 - m^2\Omega_N^2\right)\sin\left(\frac{m\pi\Omega_N}{\omega_1}\right)}{2\pi\left(m^4\Omega_N^4 - 4m^2\Omega_N^2(\omega_1^2+\omega_2^2) + 16\omega_1^2\omega_2^2\right)} ,$$

$$\kappa_{14} = \frac{\Omega_N \left(4\omega_1^2 - m^2\Omega_N^2\right)\sin\left(\frac{m\pi\Omega_N}{\omega_1}\right)}{2\pi\left(m^4\Omega_N^4 - 4m^2\Omega_N^2(\omega_1^2+\omega_2^2) + 16\omega_1^2\omega_2^2\right)}$$

$$\kappa_{15} = \frac{2\omega_1 - \Omega_N}{4\omega_1} , \qquad \kappa_{16} = \frac{\Omega_N}{4\omega_1}$$

$$\kappa_{21} = \frac{\left(m^2\Omega_N^2 - 4\omega_2^2\right)\sin\left(\frac{m\pi\Omega_N}{\omega_1}\right)}{m\pi\left(m^4\Omega_N^4 - 4m^2\Omega_N^2(\omega_1^2+\omega_2^2) + 16\omega_1^2\omega_2^2\right)} ,$$

$$\kappa_{22} = \frac{\left(m^2\Omega_N^2 - 4\omega_1^2\right)\sin\left(\frac{m\pi\Omega_N}{\omega_1}\right)}{m\pi\left(m^4\Omega_N^4 - 4m^2\Omega_N^2(\omega_1^2+\omega_2^2) + 16\omega_1^2\omega_2^2\right)} .$$

$$\kappa_{23} = \frac{\left(m^2\Omega_N^2 - 4\omega_2^2\right)\left(1 - \cos\left(\frac{m\pi\Omega_N}{\omega_1}\right)\right)}{m\pi\left(m^4\Omega_N^4 - 4m^2\Omega_N^2\left(\omega_1^2+\omega_2^2\right) + 16\omega_1^2\omega_2^2\right)} ,$$

$$\kappa_{24} = \frac{\left(m^2\Omega_N^2 - 4\omega_1^2\right)\left(1 - \cos\left(\frac{m\pi\Omega_N}{\omega_1}\right)\right)}{m\pi\left(m^4\Omega_N^4 - 4m^2\Omega_N^2\left(\omega_1^2+\omega_2^2\right) + 16\omega_1^2\omega_2^2\right)}$$

$$\kappa_{25} = \frac{1}{m\Omega_N} .$$

Appendix B: Stability charts and validation of slow-low for large stiffness asymmetry

Appendix C: Validation of the slow-flow model for large amplitude of parametric excitation ($\mathcal{O}(1)$).

Appendix D: Mode shape of cracked beam

The mode shape of the cantilever beam with single open crack is given as [28]

$$\begin{aligned}
\phi_i^1(\xi) &= (\cos\lambda_i\xi - \cosh\lambda_i\xi)\, A + (\sin\lambda_i\xi - \sinh\lambda_i\xi)\, B \\
&+ \frac{(\cosh\lambda_i + \cosh\lambda_i)\, A + (\sin\lambda_i + \sinh\lambda_i)\, B}{\frac{1}{2}\left(\lambda_i F_1 + \frac{2}{\lambda_i}\sinh\lambda_i - 2\xi_1\cosh\lambda_i\right)} \\
&\left(-\frac{\xi_1}{2}\cosh\lambda_i\xi + \frac{1}{2\lambda_i}\sinh\lambda_i\xi + \frac{\lambda_i}{4}\int_0^\xi \big(\sinh\lambda_i(\xi - s) - \sin\lambda_i(\xi - s)\big)\,|s-\xi|ds + \frac{1}{2}|\xi - \xi_1|\right),
\end{aligned} \tag{76}$$

where

$$\begin{aligned}
B =& 1 \\
A =& \frac{(\cos\lambda_i + \cosh\lambda_i) - K\,(\sin\lambda_i + \sinh\lambda_i)}{(\sin\lambda_i - \sinh\lambda_i) + K\,(\cos\lambda_i + \cosh\lambda_i)}\ , \\
K =& \frac{\lambda_i G_1 + \frac{2}{\lambda_i}\cosh\lambda_i - 2\xi_1\sinh\lambda_i}{\lambda_i F_1 + \frac{2}{\lambda_i}\sinh\lambda_i - 2\xi_1\cosh\lambda_i}\ , \\
F_1 =& \frac{\xi_1}{\lambda_i}(\cosh\lambda_i - \cos\lambda_i) + \frac{1}{\lambda_i^2}\big(\sin\lambda_i - \sinh\lambda_i + 2\sinh\lambda_i(1-\xi_1) - 2\sin\lambda_i(1-\xi_1)\big)\ , \\
G_1 =& \frac{\xi}{\lambda_i}(\sinh\lambda_i + \sin\lambda_i) + \frac{1}{\lambda_i^2}\big(\cosh\lambda_i - \cosh\lambda_i + 2\cosh\lambda_i(1-\xi_1) - 2\cos\lambda_i(1-\xi_1)\big)\ .
\end{aligned}$$

and where λ_i is the root fo the characteristics equations (detail derivations are given in Appendix : A). Mode shape of the cantilever beam without crack is given as

$$\phi_i^0(\xi) = (\cos\alpha_i\xi - \cosh\alpha_i\xi) - \left(\frac{\cos\alpha_i + \cosh\alpha_i}{\sin\alpha_i + \sinh\alpha_i}\right)(\sin\alpha_i\xi - \sinh\alpha_i\xi)\ , \tag{77}$$

where α_i is solution of

$$\cos\alpha_i + \cosh\alpha_i + 1 = 0\ . \tag{78}$$

References

[1] M. Gerber and L. Engelbrecht. The bilinear oscillator: The response of an articulated mooring tower driven by irregular seas. *Ocean Engineering*, 20(2):113–133, 1993.

[2] A. V. Dyskin, E. Pasternak, and E. Pelinovsky. Modelling resonances in topological interlocking structures. *5th Australisian Congress on Applied Mechanics (ACAM 2007)*, 10-12 December 2007, Brisbane, Australia.

[3] A. V. Dyskin, E. Pasternak, and Y. Estrin. Mortarless structures based on topological interlocking. *Frontiers of Structures and Civil Engineering*, 6(2):188–197, 2012.

[4] A. C. Lazer and P. J. McKenna. Large-amplitude periodic oscillations in suspension bridges: Some new connections with nonlinear analysis. *SIAM Review*, 32(4):537–578, 1990.

[5] S. H. Doole and S. J. Hogan. A piecewise linear suspension bridge model: Nonlinear dynamics and orbit continuation. *Dynamics and Stability of Systems*, 11(1):1–31, 1996.

[6] M. S. T. de Freitas, R. Viana, and C. Grebogi. Multistability, basin boundary structure, and chaotic behavior in a suspension bridge model: Nonlinear dynamics and orbit continuation. *Dynamics and Stability of Systems*, 14(3):927–950, 2004.

[7] M. Chati, R. Rand, and S. Mukherjee. Modal analysis of a cracked beam. *Journal of Sound and Vibration*, 207(2):249–270, 1997.

[8] K. Avramov and T. Raimberdiyev. Bifurcation behavior of bending vibrations of beams with two cracks. *Engineering Fracture Mechanics*, 178:22–38, 2017.

[9] K. Avramov and T. Raimberdiyev. Bifurcation and chaotic forced vibrations of cantilever beams with breathing cracks. *Engineering Fracture Mechanics*, 214:289–303, 2019.

[10] S. Maezawa. Superharmonic resonance in piecewise linear systems with unsymmetrical characteristics. *The 5th International Conference on Nonlinear Oscillations*, Kiev:26 Aug to 5 Sept, 1969.

[11] S. Maezewa, H. Kumano, and Y. Minakuchi. Forced vibrations in an unsymmetric piecewise linear system excited by general periodic force functions. *Bulletin of The Japan Society of Mechanical Engineers*, 23(175):68–75, 1980.

[12] T. M. J. Thompson and A. R. Bokaian. Sub-harmonic resonances and chaotic motion of a bi-linear oscillator. *IMA Journal of Applied Mathematics*, 31:207–234, 1983.

[13] S. W. Shaw and P. J. Holmes. A periodically forced piecewise linear oscillator. *Journal of Sound and Vibration*, 90(1):129–155, 1983.

[14] S. Natsiavas. On the dynamics of oscillators with bilinear damping and stiffness. *International Journal of Non-Linear Mechanics*, 25(5):535–554, 1990.

[15] S. W. Shaw. Forced vibrations of a beam with one-sided amplitude constraint: Theory and experiment. *Journal of Sound and Vibration*, 99 (2):199–212, 1985.

[16] F. F. Ehrich. Observations of sub-critical super-harmonic and chaotic responses. *ASME Journal of Vibration and Acoustics*, 114:93–100, 1992.

[17] S. Natsiavas, S. Theodossiades, and I. Goudas. Dynamic analysis of piecewise linear oscillators with time periodic coefficients. *International Journal of Non-Linear Mechanics*, 35:53–68, 2000.

[18] S. Theodossiades and S. Natsiavas. Nonlinear dynamics of gear-pair systems with periodic stiffness and backlesh. *Journal of Sound and Vibration*, 229(2):287–310, 2000.

[19] A. Marathe and A. Chatterjee. Asymmetric mathieu equations. *Proceeding of the Royal Society A*, 462:1643–1659, 2006.

[20] V. N. Belovodsky, S. L. Tsyfansky, and V. I. Beresnevich. The dynamics of a vibromachine with parametric excitation. *journal of Sound and Vibration*, 254(5):897–910, 2002.

[21] K. R. Jayaprakash and Y. Starosvetsky. Analytical study of the transition curves in the bi-linear mathieu equation. *Nonlinear Dynamics*, 101:2615–2627, 2020.

[22] K. R. Jayaprakash, V. Tandel, and Y. Starosvetsky. Dynamics of excited piecewise linear oscillators. *Nonlinear Dynamics*, 111:5513–5532, 2023.

[23] A. Kumar and Y. Starosvetsky. Analysis of transition regions in the parametrically forced system of bi-linear oscillators: Resonant excitation in the neighborhood of similar modes. *Journal of Sound and Vibration*, 515:116435, 2021.

[24] A. Kumar, Y. Starosvetsky, and K. R. Jayaprakash. Analysis of transition resions of bilinear, parametrically driven, two-oscillator model: Resonance excitation in the neighborhood of non-similar nnms. *International Journal of Nonlinear Mechanics*, 145:104074, 2022.

[25] A.F. Filippov. *Differential Equations with Discontinuous Righthand Sides. Mathematics and Its Applications (Soviet Series)*, volume 18. Kluwer Academic, Boston, 1988.

[26] T. G. Chondros and A. D. Dimarogonas. Identification of cracks and welded joint of complex structures. *Journal of Sound and Vibration*, 69(4):531–538, 1980.

[27] P. F. Rizos and N. Aspragathos. Identification of crack location and magnitude in a cantilever beam from the vibration modes. *Journal of Sound and Vibration*, 138(3):381–388, 1990.

[28] E. I. Shufrin and R. Ruotolo. Natural frequencies of a beam with an arbitrary number of cracks. *Journal of Sound and Vibration*, 222(3):409–423, 1999.

[29] S. Caddemi and I. Calió. Exact closed-form solution for the vibration modes of the euler-bernoulli beam with multiple open cracks. *Journal of Sound and Vibration*, 327:473–489, 2009.

[30] S. Maiti, A. Kumar, and H. Kanchwala. Dynamics of a cantilever beam with solitary open crack: nonlinear response to external and base excitation. *Nonlinear Dynamics*, 113:7901–7936, 2025.

[31] S. Malyshev and K. Avramov. Nonlinear normal modes and bifurcations of geometrically nonlinear vibrations of beams with breathing crackss. *Acta Mechanica*, 236:1317–1337, 2025.

[32] J. Wang and P. Qiao. Vibration of beams with arbitrary discontinuities and boundary conditions. *Journal of Sound and Vibration.*, 308:12–27, 2007.

[33] A. H. Nayfeh and P. F. Pai. Linear and nonlinear structural mechanics. *WILEY-VCH VerlagGmbH and Co. KGaA*, 2004.

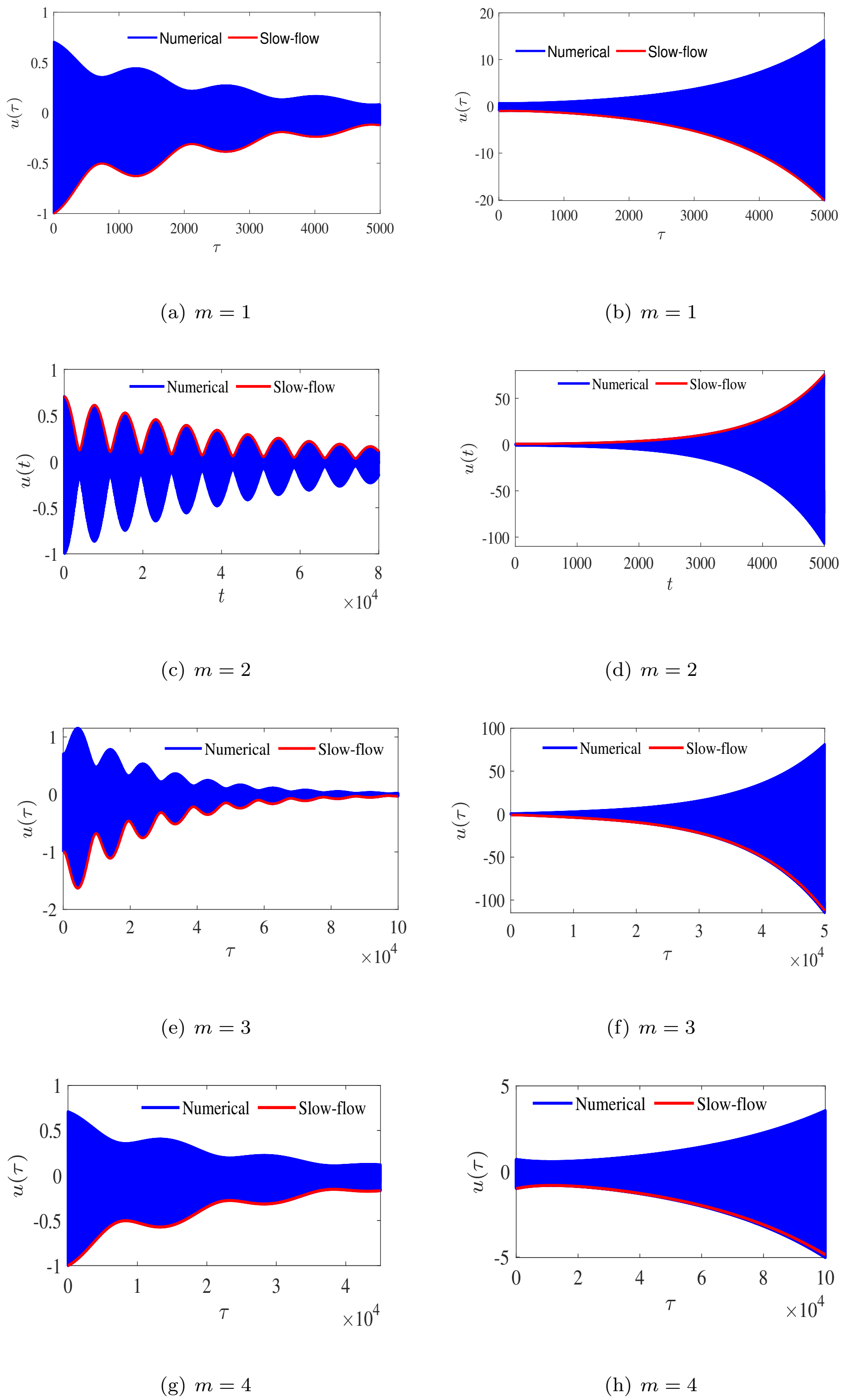

Figure 1: Verification of the slow-flow model obtained using the method of averaging against the full model for two resonance condition $1:1$, $2:1$, $3:1$ and $4:1$, respectively. The amplitudes of parametric excitation are selected to illustrate bounded (left column) and unbounded (right column) responses for the $1:1$ and $2:1$ resonance conditions, respectively. Other parameters are $\delta^2 = 2$, $\lambda_0 = 0.001$, $\lambda_2 = 0.0005$, $\epsilon = 0.1$ and other parameters, e.g., P_0, P_1 and σ are taken from the neighborhood of the transition curves corresponding to each resonance condition .

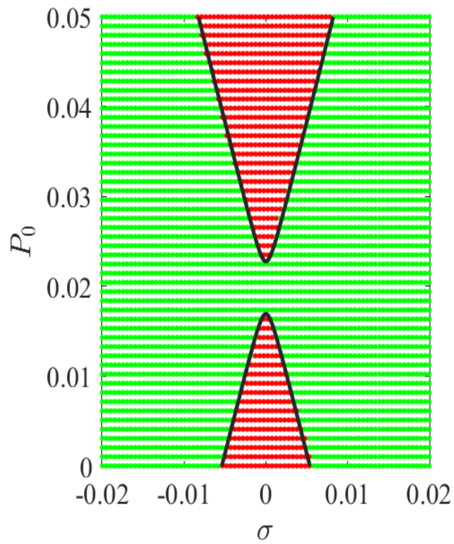

(a) $\lambda_0 = 0.001$, $\lambda_1 = 0.0005$

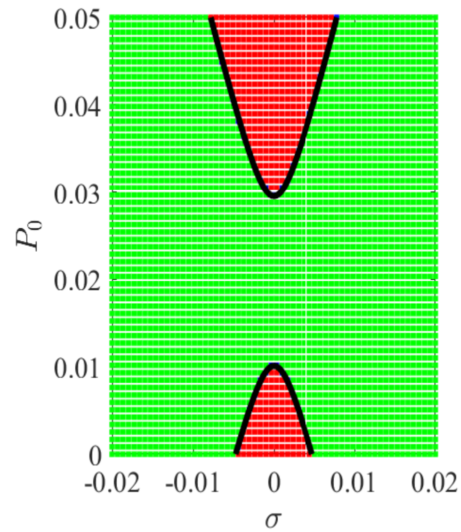

(b) $\lambda_0 = 0.001$, $\lambda_1 = 0.005$

Figure 2: The stability charts (for resonance condition $1:1$) are shown in the plane of excitation amplitude (P_0) corresponding to one state (i.e. $u(\tau) > 0$) and detuning parameter (σ) while keeping excitation amplitude (P_1) corresponding to the other state (i.e., $u(\tau) < 0$)) as a fixed value. Here green and red regions represent stable and unstable regions, respectively, obtained using numerical integration of the full model given in Eqs. (6) and (7) and thick black lines represent transition curves obtained analytically using a close-form expression in Eq. (36). The effect of damping on the stability has also been shown with low damping (left) and high damping (right). The space between the upper and lower tongues increases with damping. Other parameters are $\delta^2 = 2$, $\epsilon = 0.1$ and $P_1 = 0.05$.

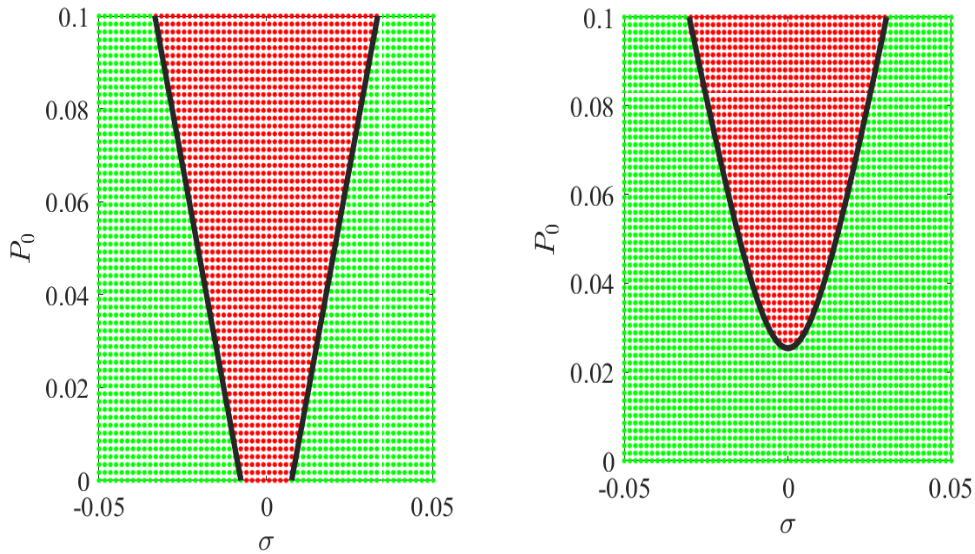

(a) $\lambda_0 = 0.001$, $\lambda_1 = 0.005$

(b) $\lambda_0 = 0.01$, $\lambda_1 = 0.02$

Figure 3: The stability charts (for resonance condition $2:1$) are shown in the plane of excitation amplitude (P_0) corresponding to one state (i.e. $u(\tau) > 0$) and detuning parameter (σ) while keeping excitation amplitude (P_1) corresponding to the other state (i.e., $u(\tau) < 0$)) as a fixed value. Here green and red regions represent stable and unstable regions, respectively, obtained using numerical integration of the full model given in Eqs. (6) and (7) and thick black lines represent transition curves obtained analytically using a close-form expression in Eq. (36). The effect of damping on the stability has also been shown with low damping (left) and high damping (right). The space between the upper and lower tongues increases with damping. Other parameters are $\delta^2 = 2$, $\epsilon = 0.1$ and $P_1 = 0.05$.

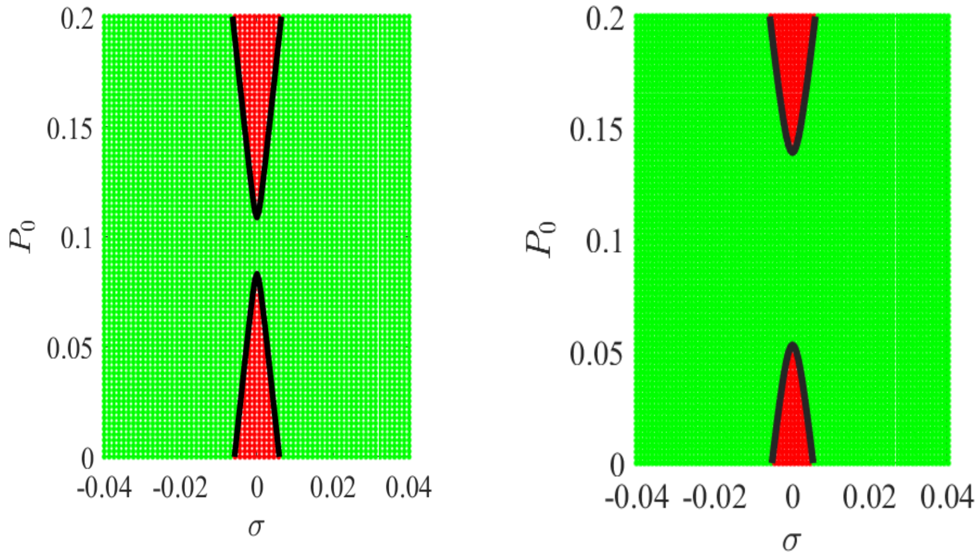

(a) $\lambda_0 = 0.001$, $\lambda_2 = 0.0005$

(b) $\lambda_0 = 0.001$, $\lambda_1 = 0.005$

Figure 4: The stability charts (for resonance condition $3:1$) are shown in the plane of excitation amplitude (P_0) corresponding to one state (i.e. $u(\tau) > 0$) and detuning parameter (σ) while keeping excitation amplitude (P_1) corresponding to the other state (i.e., $u(\tau) < 0$)) as a fixed value. Here green and red regions represent stable and unstable regions, respectively, obtained using numerical integration of the full model given in Eqs. (6) and (7) and thick black lines represent transition curves obtained analytically using a close-form expression in Eq. (36). The effect of damping on stability has also been shown with low damping (left) and high damping (right). The space between the upper and lower tongues increases with damping. Other parameters are $\delta^2 = 2$, $\epsilon = 0.1$ and $P_1 = 0.05$.

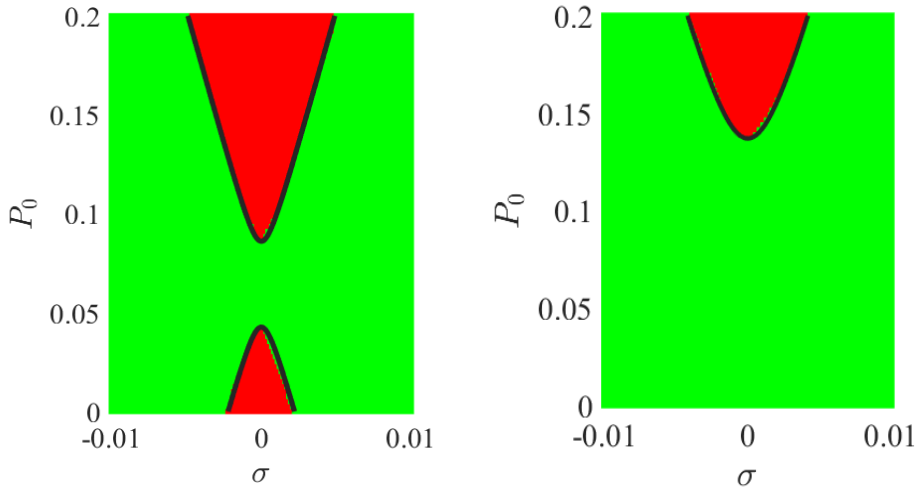

(a) $\lambda_0 = 0.001$, $\lambda_2 = 0.0005$

(b) $\lambda_0 = 0.001$, $\lambda_1 = 0.005$

Figure 5: The stability charts (for resonance condition $4:1$) are shown in the plane of excitation amplitude (P_0) corresponding to one state (i.e. $u(\tau) > 0$) and detuning parameter (σ) while keeping excitation amplitude (P_1) corresponding to the other state (i.e., $u(\tau) < 0$)) as a fixed value. Here green and red regions represent stable and unstable regions, respectively, obtained using numerical integration of the full model given in Eqs. (6) and (7) and thick black lines represent transition curves obtained analytically using a close-form expression in Eq. (36). The effect of damping on the stability has also been shown with low damping (left) and high damping (right). The space between the upper and lower tongues increases with damping. Other parameters are $\delta^2 = 2$, $\epsilon = 0.1$ and $P_1 = 0.05$.

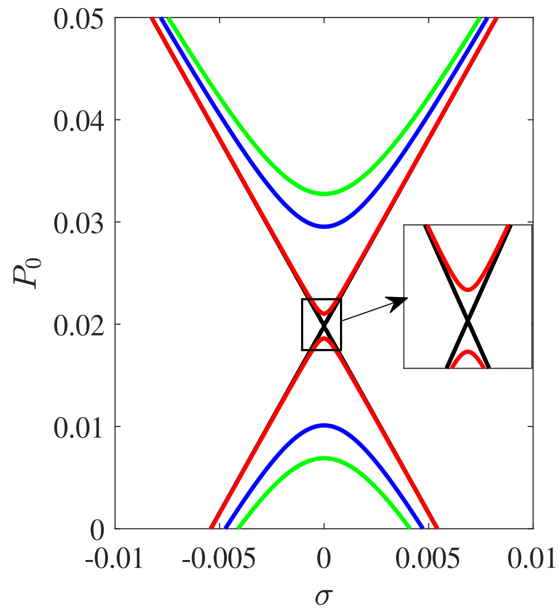

Figure 6: Variation of the transition curves (analytically) with damping parameters ($\lambda_0 = \lambda_1 = 0$ (**black**), $\lambda_1 = 0.0002,\ \lambda_2 = 0.0005$ (**red**), $\lambda_1 = 0.001,\ \lambda_2 = 0.005$ (**blue**) and $\lambda_1 = 0.002,\ \lambda_2 = 0.005$ (**green**)), and resonance condition is $1:1$ and $P_1 = 0.05$.

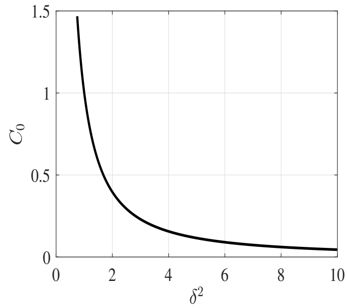

(a) $m = 1$

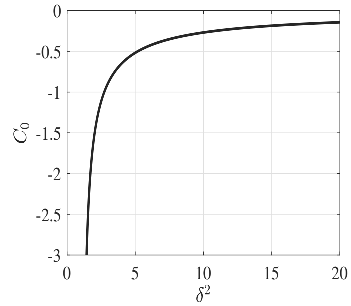

(b) $m = 2$

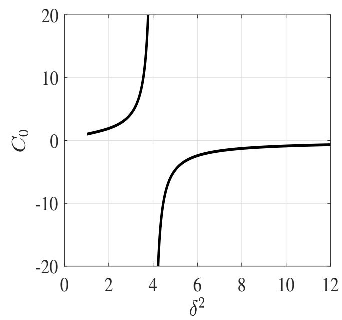

(c) $m = 3$

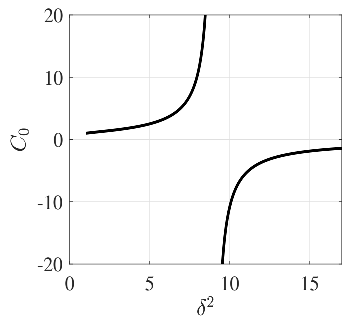

(d) $m = 4$

Figure 7: Variation of constant C_0 with system parameter (δ^2) and resonance conditions ($m : 1$). Here C_0 provide information about the crossing point, i.e., the crossing points of transition curves (with zero damping) using Eq. (37), e.g. as shown in Fig. 6

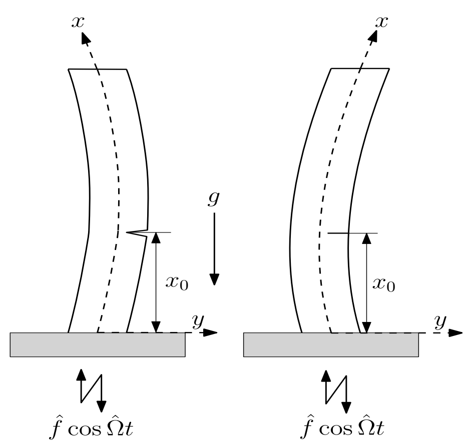

(a) Open (b) Closed

Figure 8: Schematic diagram of the based excited cantilever beam with breathing crack

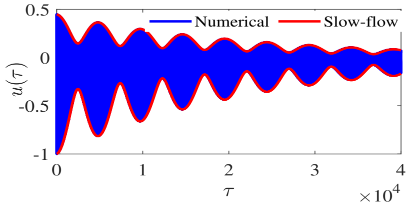

(a) $P_0 = 0.05,\ \sigma = 0.02,\ m = 1$

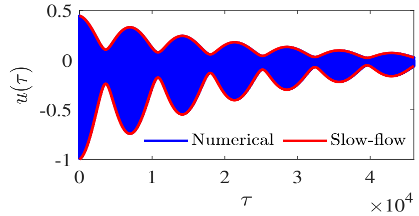

(b) $P_0 = 0.05,\ \sigma = 0.017,\ m = 2$

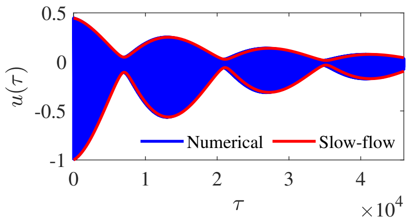

(c) $P_0 = 0.05,\ \sigma = 0.016,\ m = 1$

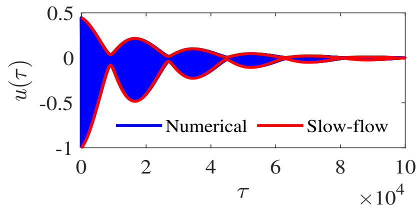

(d) $P_0 = 0.05,\ \sigma = 0.015,\ m = 2$

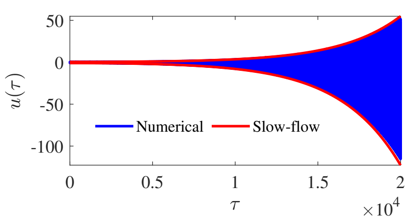

(e) $P_0 = 0.05,\ \sigma = 0.014,\ m = 1$

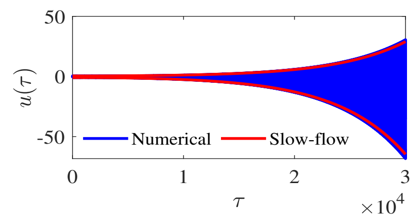

(f) $P_0 = 0.05,\ \sigma = 0.014,\ m = 2$

Figure 9: Verification of the slow-flow model obtained through the method of averaging is carried out by comparison with the full-order model for the 1:1 and 2:1 resonance conditions. The selected amplitudes of parametric excitation illustrate bounded and unbounded responses for the $1:1$ (left column) and $2:1$ (right column) resonance cases, respectively. Two distinct initial conditions are considered in the slow-flow model to recover the upper and lower envelopes of the numerical solutions. The parameter combinations $(P_1,\ P_0\ \sigma)$ are extracted from the corresponding instability charts presented in Fig. 10 in the neighborhood of the transition curves. The close agreement between the slow-flow and full-order responses validates the effectiveness of the averaging approximation within the considered parameter regime. Other parameters are $\delta^2 = 5$, $\lambda_0 = 0.001$, $\lambda_2 = 0.0005$, $\epsilon = 0.1$, $P_1 = 0.05$.

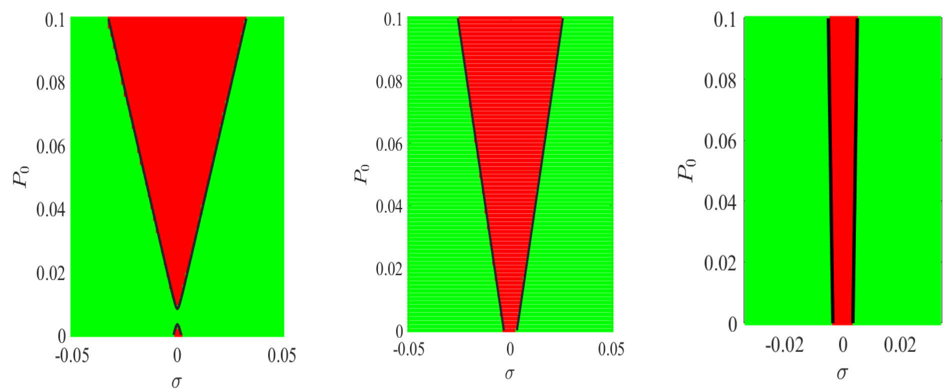

(a) $m = 1$

(b) $m = 2$

(c) $m = 2$

Figure 10: The stability charts (for resonance conditions $1:1,\ 2:1,\ 3:1$) are shown in the plane of excitation amplitude (P_0) corresponding to one state (i.e. $u(\tau) > 0$) and detuning parameter (σ) while keeping excitation amplitude (P_1) corresponding to the other state (i.e., $u(\tau) < 0$)) as a fixed value. Here green and red regions represent stable and unstable regions, respectively, obtained using numerical integration of full model given in Eqs. (6) and (7) and thick black lines represent transition curves obtained analytically using close form expression in Eq. (36). Other parameters are $\delta^2 = 5$, $\epsilon = 0.1$ and $P_1 = 0.05$.

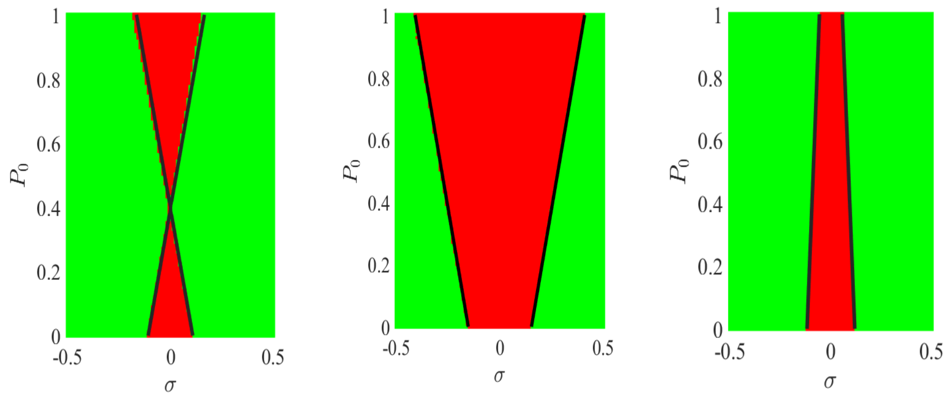

(a) $m = 1$ (b) $m = 2$ (c) $m = 3$

Figure 11: The stability charts (for resonance conditions $1:1,\ 2:1,\ 3:1$) are shown in the plane of excitation amplitude (P_0) corresponding to one state (i.e. $u(\tau) > 0$) and detuning parameter (σ) while keeping excitation amplitude (P_1) corresponding to the other state (i.e., $u(\tau) < 0$)) as a fixed value for for large amplitudes of excitation, i.e., $\mathcal{O}(1)$. Here green and red regions represent stable and unstable regions, respectively, obtained using numerical integration of the full model given in Eqs. (6) and (7) and thick black lines represent transition curves obtained analytically using a close-form expression in Eq. (36). Parameters are $\delta^2 = 2$, $\lambda_0 = 0.001$, $\lambda_2 = 0.0005$, $\epsilon = 0.1$ and $P_1 = 1$.

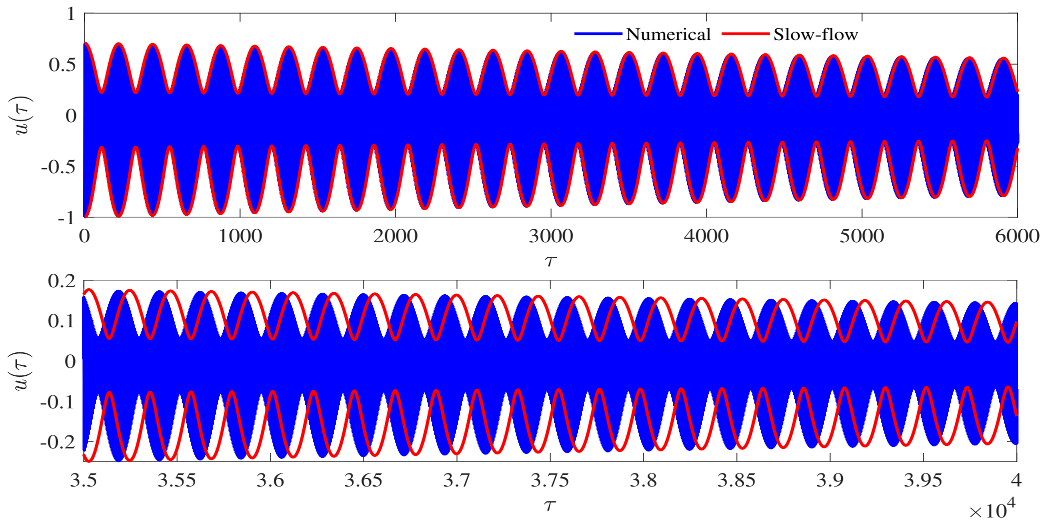

(a) $m = 2,\ P_0 = 1,\ P_1 = 1\ \sigma = 0.5$

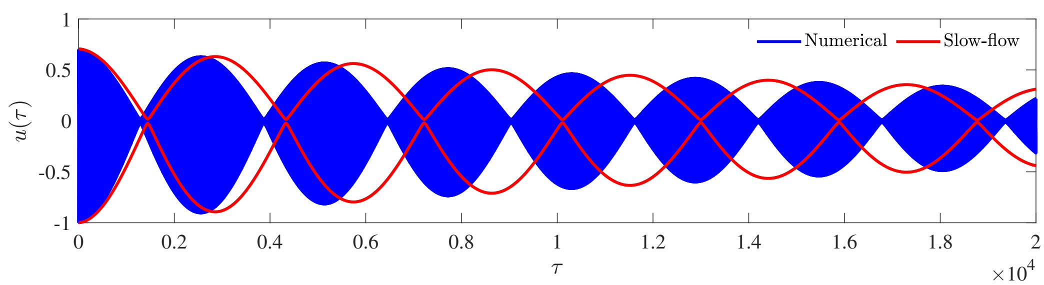

(b) $m = 2\ ,\ P_0 = 1,\ P_1 = 1\ \sigma = 0.41$

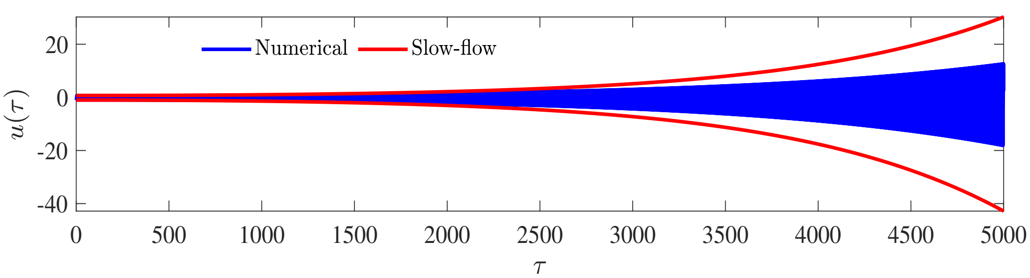

(c) $m = 2,\ P_0 = 1,\ P_1 = 1\ \sigma = 0.409$

Figure 12: Verification of the slow-flow model obtained using the method of averaging against the full model for two resonance condition $2:1$, respectively for $P_0,\ P_1 = \mathcal{O}(1)$. The amplitudes of parametric excitation are selected to illustrate bounded and unbounded responses for the $1:1$ and $2:1$ resonance conditions, respectively. Other parameters are $\delta^2 = 2$, $\lambda_0 = 0.001$, $\lambda_2 = 0.0005$, $\epsilon = 0.1$. The figures show that, for large excitation amplitudes, i.e., $(P_0, P_1 = \mathcal{O}(1))$, the averaged slow-flow model deviates quantitatively from the response of the full model. However, it still captures the qualitative dynamic behavior of the system, accurately reproducing the overall response characteristics and bifurcation trends.